Three-Phase Compositional Modeling With Capillarity in Heterogeneous and Fractured Media

Joachim Moortgat,* SPE, and **Abbas Firoozabadi,** SPE, Reservoir Engineering Research Institute

Summary

We model for the first time capillarity in fully compositional three-phase flow, with higher-order finite-element (FE) methods. Capillary pressure gradients may be an important driving force, particularly in layered or fractured porous media, which exhibit sharp discontinuities in permeability. We introduce a simple local computation of the capillary pressure gradients, propose a fractional-flow formulation in terms of the total flux, and resolve complications arising from gravity and capillarity in the upwinding of phase fluxes. Fractures are modeled with the crossflow equilibrium concept, which allows large timesteps and includes all physical interactions between fractures and matrix blocks. The pressure and flux fields are discretized by the mixed hybrid finite-element method, and mass transport is approximated by a higher-order local discontinuous Galerkin (DG) method. Numerical-dispersion and grid-orientation effects are significantly reduced, which allows computations on coarser grids and with larger timesteps. The main advantages in the context of this work are the accurate pressure gradients and fluxes at the interface between regions of different permeabilities. The phase compositions are computed with state-of-the-art phase-splitting algorithms and stability analyses to guarantee the global minimum of Gibbs free energy. Accurate compositional simulation motivates the use of an implicit-pressure/explicit-composition (IMPEC) scheme, and we discuss the associated Courant-Friedrichs-Lewy (CFL) condition on the timesteps. We present various numerical examples on both core- and large-scale, illustrating the capillary end effect, capillary-driven crossflow in layered media, and the importance of capillarity in fractured media for three-phase flow.

Introduction

Multiphase flow in porous media is driven by viscous, gravitational, diffusive, and capillary forces. For high flow rates in homogeneous media, the latter three forces play a relatively small role. However, even in homogeneous media the interplay between the various forces may be important. Displacement fronts may be unstable to viscous or gravitational instabilities, resulting in fingering. Such fingers may be stabilized by Fickian diffusion, which is driven by compositional gradients, and either stabilized or enhanced by capillarity, which is driven by saturation gradients. In some cases, diffusion and capillarity are critical in heterogeneous media, in which steep compositional and saturation gradients generally develop in the domain. Depending on the flow rate, capillarity or diffusion may be the main driving force in fractured or intensively layered domains (Yokoyama and Lake 1981).

In past work (Moortgat et al. 2009; Moortgat and Firoozabadi 2010; Moortgat et al. 2013), we have investigated Fickian diffusion in heterogeneous and fractured media. Capillarity was neglected because the focus was on CO_2 injection, which has a low surface tension and considerable species transfer with the oil phase at most reservoir conditions. More recently, we have presented a compositional model for three-phase flow (Moortgat et al. 2011, 2012), motivated by an interest in improved oil recovery by CO_2 injection in reservoirs with a high connate or residual water saturation, and in the water-alternating-gas (WAG) process. For the aqueous phase in particular, the surface tension may be high and capillarity must be considered. In various applications, such as coreflooding, the gas/oil capillary pressure may have a significant impact as well. One example is the capillary end effect in drainage of oil by gas injection: Because the capillary pressure is (nearly) zero at a producing outlet and inside fractures, the associated capillary pressure gradients result in oil saturations remaining considerably above the residual oil saturation (ROS), particularly at low injection rates (Hadley and Handy 1956). In three-phase flow, each of the capillary-driven fluxes depends indirectly on all three phase saturations.

In this work, we present for the first time the formulation for capillarity in fully compositional three-phase flow, with higher-order FE methods in an IMPEC scheme. Pressures and fluxes are computed simultaneously by the mixed hybrid FE (MHFE) method, and to the same order accuracy. Mass transport is approximated by a higher-order DG method. This combination of FE methods is a particularly natural choice for heterogeneous media, in which phase properties may exhibit sharp jumps at the discontinuities in permeability, whereas pressures and fluxes are continuous. The methods naturally accommodate a permeability tensor and can be readily implemented on complex unstructured grids. Moreover, the higher-order accuracy is required to resolve small-scale viscous and gravitational instabilities, which may be suppressed by numerical dispersion in traditional lowest-order finite-difference (FD) methods. The robustness and accuracy of the MHFE-DG method has been extensively demonstrated in our earlier work, as well as by Hoteit and Firoozabadi (2005, 2006a, b) for single- and two-phase compositional flow without capillarity, and for incompressible two-phase flow with capillarity in homogeneous and fractured domains in Hoteit and Firoozabadi (2008a, b). To model fractures, we adopt the crossflow equilibrium concept (Tan and Firoozabadi, 1995a, b), which combines fractures with a small neighborhood in the matrix into large computational elements. This approach facilitates large timesteps and retains the advantage of single-porosity models in treating all physical interactions between fractures and the matrix the same as in unfractured domains. Any configuration of discrete fractures can be modeled, unlike the sugar-cube configuration in dual-porosity models [although this restriction may be relaxed (Moinfar et al. 2012)]. Several discrete fracture approaches are compared for a three-phase black-oil model in Geiger et al. (2009).

In compositional multiphase flow, capillarity considerably complicates the problem because of the high degree of additional nonlinearity caused by the strong saturation and composition dependence of the capillary pressures. We present a local computation of the capillary pressure gradients from cell-centered capillary pressures and the harmonic average of an effective phase mobility, on the basis of first-principle derivations. The approach allows for discontinuous capillary pressure gradients, mobilities, and saturations at element edges, but guarantees a continuous capillary pressure and flux across edges. We propose a fractional-flow formulation, in which we solve directly only for the total flux. The subsequent construction of the phase fluxes from the

* Currently at School of Earth Sciences, Ohio State University.

This paper (SPE 159777) was accepted for presentation at the SPE Annual Technical Conference and Exhibition, San Antonio, Texas, USA, 8–10 October 2012, and revised for publication. Original manuscript received for review 13 November 2012. Revised manuscript received for review 24 January 2013. Paper peer approved 31 January 2013.

total flux is a challenge when the flux consists of viscous, capillary, and gravitational terms that allow countercurrent flow. We present a new elegant scheme in this work that overcomes these complications, and discuss various other subtleties in the modeling of capillarity for multiphase compositional flow.

In the following sections, we discuss the problem formulation and numerical implementation and present six numerical examples to illustrate important features related to capillarity, such as the capillary end effect; imbibition and drainage in layered media, both parallel and perpendicular to the layers; and imbibition and drainage in fractured domains.

Mathematical Formulation

The equations in this section hold in both the fractures and matrix. An efficient discrete fracture discretization is discussed in the following.

Pressures and Fluxes. The flow of water (w), oil (o), and gas (g) in porous media is described by Darcy's law for each of the phases:

$$\boldsymbol{u}_\alpha = -\frac{k_{r\alpha}}{\mu_\alpha}\mathrm{K}(\nabla p_\alpha - \rho_\alpha \boldsymbol{g}), \quad \alpha = w, o, g, \quad \ldots\ldots\ldots\ldots (1)$$

where K is the absolute-permeability tensor of the porous medium; $k_{r\alpha}$, μ_α, and ρ_α are the relative permeability, viscosity, and mass density of phase α, respectively; $\boldsymbol{g}$ is the gravitational vector (positive in the downward direction), and p_α is the pressure associated with each phase. In fractured media, different absolute and relative permeabilities are used in the fracture and matrix elements. In homogeneous media, capillarity may often be neglected and $p = p_w = p_o = p_g$. In this work, we consider flow through more-complicated heterogeneous and fractured media with capillarity. We define capillary pressures as

$$p_{c,go} = p_g - p_o \quad \ldots\ldots\ldots\ldots\ldots\ldots\ldots\ldots (2)$$

$$p_{c,wo} = p_o - p_w. \quad \ldots\ldots\ldots\ldots\ldots\ldots\ldots\ldots (3)$$

A third capillary pressure can be expressed in terms of the preceding definitions as $p_{c,gw} = p_g - p_w = p_{c,go} + p_{c,wo}$. In the flow equations, we choose to work with $p_{c,go}$, $p_{c,wo}$, and the oil pressure p_o as a reference. Eq. 1 can be written in terms of the capillary pressures as

$$\boldsymbol{u}_g = -\frac{k_{rg}}{\mu_g}\mathrm{K}(\nabla p_o + \nabla p_{c,go} - \rho_g \boldsymbol{g}) \quad \ldots\ldots\ldots\ldots (4)$$

$$\boldsymbol{u}_o = -\frac{k_{ro}}{\mu_o}\mathrm{K}(\nabla p_o - \rho_o \boldsymbol{g}) \quad \ldots\ldots\ldots\ldots\ldots\ldots (5)$$

$$\boldsymbol{u}_w = -\frac{k_{rw}}{\mu_w}\mathrm{K}(\nabla p_o - \nabla p_{c,wo} - \rho_w \boldsymbol{g}). \quad \ldots\ldots\ldots\ldots (6)$$

The capillary pressures in Eqs. 4 and 6 depend on two of the phase saturations S_α, and (through the surface tension and wettability) on the phase molar densities c_α and molar composition $x_{i,\alpha}$, with i being the index labeling species:

$$p_{c,go} = p_{c,go}(S_\alpha, c_\alpha, x_{i,\alpha}), \ \alpha = g, o; \ \ i = 1, \ldots n_c - 1, \quad \ldots. (7)$$

$$p_{c,wo} = p_{c,wo}(S_\alpha, c_\alpha, x_{i,\alpha}), \ \alpha = o, w; \ \ i = 1, \ldots n_c - 1. \quad \ldots (8)$$

The oil pressure is solved from the pressure equation by Acs et al. (1985) and Watts (1986):

$$\phi\kappa_T \frac{\partial p_o}{\partial t} + \sum_{i=1}^{n_c} \bar{v}_i(\nabla \cdot \boldsymbol{U}_i - F_i) = 0 \quad \ldots\ldots\ldots\ldots\ldots (9)$$

$$\boldsymbol{U}_i = \sum_\alpha (c_\alpha x_{i,\alpha} \boldsymbol{u}_\alpha + S_\alpha \boldsymbol{J}_{i,\alpha}), \quad i = 1, \ldots, \ n_c, \quad \ldots\ldots\ldots (10)$$

where ϕ is the porosity and κ_T represents the total compressibility of the three-phase mixture and the formation. When formation compressibility is significant, ϕ and κ_T depend on pressure. The total partial molar volume of each species in the mixture is denoted by $\bar{v}_i$. Expressions for κ_T and $\bar{v}_i$ in three-phase were presented in Moortgat et al. (2012) and are evaluated in this work with respect to the oil pressure. Diffusive fluxes are denoted by $\boldsymbol{J}_{i,\alpha} = \boldsymbol{J}_{i,\alpha}(T, p_o, x_{1,\alpha}, \ldots, x_{n_c-1,\alpha})$ and are computed from the full matrix of composition-dependent diffusion coefficients in Moortgat and Firoozabadi (2010). T is the temperature, which is assumed constant in this work. The $\boldsymbol{u}_\alpha$ term in Eq. 10 describes the convective fluxes. Sink and source terms, which may represent injection and production wells, are gathered in F_i.

Solving for all three phase fluxes in Eq. 4 individually is computationally expensive, and is complicated by the fact that each of the phase mobilities, denoted as $\lambda_\alpha = k_{r\alpha}/\mu_\alpha$, may vanish. Instead, we solve directly for the total flux $\boldsymbol{u}_t = \Sigma_\alpha \ \boldsymbol{u}_\alpha$. The notation throughout this formulation is simplified by defining the effective phase mobilities $\mathrm{k}_\alpha = \mathrm{K}\lambda_\alpha$, the total effective mobility $\mathrm{k}_t = \Sigma_\alpha \ \mathrm{k}_\alpha$, and the fractional-flow functions $f_\alpha = \mathrm{k}_\alpha/\mathrm{k}_t$.

Summing the three equations in Eqs. 4 through 6, we find a single relation for the total flux:

$$\boldsymbol{u}_t = -\mathrm{k}_t(\nabla p_o - f_w \nabla p_{c,wo} + f_g \nabla p_{c,go} - \sum_\alpha f_\alpha \rho_\alpha \boldsymbol{g}) \quad \ldots. (11)$$

The fractional-flow formulation has the advantage that the total effective mobility k_t is positive definite, such that Eq. 11 can be inverted in terms of ∇p_o and solved together with Eq. 9.

Once the total flux $\boldsymbol{u}_t$ is known, the phase fluxes can be constructed, independent of p_o, by

$$\boldsymbol{u}_\alpha = f_\alpha(\boldsymbol{u}_t - \boldsymbol{G}_\alpha), \text{ with}$$
$$\begin{cases} \boldsymbol{G}_g &= \sum_\alpha \tilde{\mathrm{k}}_\alpha(\rho_\alpha - \rho_g)\mathbf{g} + \tilde{\mathrm{k}}_w \nabla p_{c,wo} + (\tilde{\mathrm{k}}_o + \tilde{\mathrm{k}}_w)\nabla p_{c,go} \\ \boldsymbol{G}_o &= \sum_\alpha \tilde{\mathrm{k}}_\alpha(\rho_\alpha - \rho_o)\boldsymbol{g} + \tilde{\mathrm{k}}_w \nabla p_{c,wo} - \tilde{\mathrm{k}}_g \nabla p_{c,go} \\ \boldsymbol{G}_w &= \sum_\alpha \tilde{\mathrm{k}}_\alpha(\rho_\alpha - \rho_w)\boldsymbol{g} - (\tilde{\mathrm{k}}_g + \tilde{\mathrm{k}}_o)\nabla p_{c,wo} - \tilde{\mathrm{k}}_g \nabla p_{c,go} \end{cases}, \quad \ldots\ldots\ldots\ldots\ldots (12)$$

with $\tilde{\mathrm{k}}_\alpha$ the effective phase mobility upwinded with respect to $\boldsymbol{u}_\alpha$. Determining the upwind direction for $\tilde{\mathrm{k}}_\alpha$ when the phase fluxes are not known is the most challenging part of this formulation and is discussed below.

In fractured media, fractures are combined with a small neighborhood in the matrix into larger computational elements (discussed later). For these elements, Eq. 11 is computed for both the fracture and the matrix contributions to the flux.

Mass Balance. Species balance is guaranteed by the mass-conservation equation in terms of the total molar density c and overall molar composition of the three-phase mixture, z_i

$$\phi \frac{\partial c z_i}{\partial t} + \nabla \cdot \boldsymbol{U}_i = F_i, \quad i = 1, \ldots, n_c. \quad \ldots\ldots\ldots\ldots (13)$$

Thermodynamic Equilibrium. Thermodynamic equilibrium requires the equality of fugacities of each of the species i in all three phases α. We neglect the effect of capillary pressure on the phase behavior by performing all phase-split computations on the basis of the oil pressure. This assumption should be relaxed for nano-pores, in which the capillary pressure may be large compared with the oil pressure. Choosing oil as a reference phase, we define the equilibrium ratios $K_{i,g} = x_{i,g}/x_{i,o}$ and $K_{i,w} = x_{i,w}/x_{i,o}$. Equality of fugacities is equivalent to the relations:

$$\ln K_{i,\alpha} = \ln\varphi_{i,o} - \ln\varphi_{i,a}, \quad i = 1, \ldots, n_c; \quad \alpha = g, w. \quad \ldots. (14)$$

The molar fractions of each phase, β_α, can be found from

$$\sum_\alpha \beta_\alpha = 1 \quad \text{and} \quad z_i = \sum_\alpha \beta_\alpha x_{i,\alpha}, \quad i = 1, \ldots, n_c. \quad \ldots. (15)$$

The overall and phase molar compositions are not independent and satisfy the constraints

$$\sum_i z_i = \sum_i x_{i,g} = \sum_i x_{i,o} = \sum_i x_{i,w} = 1. \quad \ldots\ldots\ldots (16)$$

The phase molar densities are obtained from

$$c_\alpha = \frac{p_\alpha}{Z_\alpha RT} + VSP_\alpha, \quad \ldots\ldots\ldots\ldots\ldots\ldots\ldots (17)$$

with R the universal gas constant and VSP_α an empirical volume shift parameter to improve the accuracy of the density of phase α. VSP_α is taken as the same for both oil and gas phases in this work to improve the reliability in the near-critical region. Z_α is the compressibility factor of phase α. For phases without associating species (gas and oil), Z_α is given by the cubic Peng-Robinson (PR) equation of state (EOS). For the aqueous phase, Z_α is obtained from the cubic-plus-association (CPA) EOS, which accounts for cross-association between CO_2 and water molecules and self-association of water. In the absence of water, the CPA-EOS reduces to the PR-EOS. Challenges associated with the three-phase stability analysis and phase-split routines are the subject of a recent paper (Moortgat et al. 2012).

Boundary Conditions. The preceding equations (Eqs. 1–17) are solved for the unknown phase pressures p_α, fluxes $\boldsymbol{u}_\alpha$, compositions $x_{i,\alpha}$, and mole fraction of each phase β_α, as well as the total molar density c and composition z_i of the mixture. The problem statement is completed by initial and boundary conditions. We prescribe either fully impermeable boundaries with all injection and production wells described by sink/source terms in F_i (specifying injection and production rates), or we consider a constant pressure in the production wells, which implies nonoverlapping Dirichlet (in production wells) and Neumann (everywhere else) boundary conditions. Boundary conditions can be changed during simulations, such as when switching from depletion (constant production rate) to water or gas injection at a constant pressure, or when turning injection and production wells on or off in different locations. The initial condition is specified by a pressure field and composition throughout the domain.

Numerical Implementation With Higher-Order Methods

The flow equations are solved by higher-order FE methods and an IMPEC scheme. Specifically, the mass-transport equation, Eq. 13, is discretized by the local DG method. Darcy's equation for the total flux, Eq. 11, and the pressure equation for p_o are solved simultaneously, and to the same order accuracy by the MHFE method. We have successfully developed and tested this combination of higher-order methods before for three-phase compositional flow in homogeneous and fractured media (Moortgat et al. 2011, 2012; Moortgat and Firoozabadi 2012), but neglecting capillarity. In the following sections, we will highlight unique features of the model and specific challenges encountered in incorporating capillarity in the model. We refer to earlier work where the proposed implementation is similar.

DG Mass-Transport Update. We use a linear DG approximation on triangular elements and a bilinear DG approximation on rectangular elements. The overall and phase compositions are updated at either all nodes or all edge centers of each element. Like other higher-order methods, the DG method considerably reduces numerical dispersion, which allows the use of coarse grids and larger timesteps. This is particularly important when capillarity and Fickian diffusion are included, because these terms incur stringent constraints on the timesteps in an IMPEC scheme (discussed later in this paper). More important, in the context of this work, is the discontinuous nature of the DG method. At each edge, two different values of the state variables (e.g., composition, density, saturation) are defined, one on either side. This is a crucial feature in the treatment of heterogeneous, layered, and fractured domains, in which these variables show sharp discontinuities at the boundaries between regions of different permeability (and porosity). The mass-conservation equation, Eq. 13, has the same form as when capillarity is neglected, and the DG implementation is identical to that in Moortgat et al. (2011).

Mixed FE Method for Fluxes and Pressures. In this subsection, we describe the MHFE implementation for unfractured 2D domains. The extension to fractures is discussed in the next section.

The first step in the MHFE method is to decompose fluxes into their normal components across edges E of each mesh element K with boundary ∂K. We introduce the lowest-order Raviart-Thomas basis vector fields $\boldsymbol{w}_{K,E}$ ($\mathbf{x} = x, y$) (Raviart and Thomas 1977), which satisfy $\boldsymbol{w}_{K,E} \cdot \boldsymbol{n}_{K,E'} = 1/|E|$ and $\nabla \cdot \boldsymbol{w}_{K,E} = 1/|K|$. In two dimensions, $|K|$ and $|E|$ are the cell area and edge length, respectively. The decomposed fluxes are constructed as $\boldsymbol{u}_t(t,\boldsymbol{x}) = \sum_{E\in\partial K} q_{K,E}(t)\boldsymbol{w}_{K,E}(\boldsymbol{x})$, and similarly for phase fluxes $\boldsymbol{u}_\alpha$ and $\mathrm{k}_g \nabla p_{c,go}(t,\boldsymbol{x}) \to q^c_{go,K,E}$, $\mathrm{k}_w \nabla p_{c,wo}(t,\boldsymbol{x}) \to q^c_{wo,K,E}$, $\phi S_\alpha \boldsymbol{J}_{i,\alpha}(t,\boldsymbol{x}) \to q^{\mathrm{diff}}_{i,\alpha,K,E}$, and $\boldsymbol{g}(\boldsymbol{x}) \to q^g_{K,E}$. We chose not to include $\Sigma_\alpha \mathrm{k}_{\alpha,K}\rho_{\alpha,K}$ in the last definition for notational convenience in the discussion of fractures in the next section.

In the next step, Darcy's law for the total flux (Eq. 11) is put in weak form by multiplying by $\boldsymbol{w}_{K,E}$ and integrating over K. The pressure gradient is integrated by parts, and the coefficients are assumed to be element-wise constant. We define the element-averaged oil pressure $p_{o,K} = \int_K p_o$ and the edge-averaged oil pressures $\int_{\partial K} p_o = \Sigma_E \int_E p_o = \Sigma_E t p_{o,K,E}$. The discretized Darcy law takes the form

$$q_{K,E} = \theta_{K,E} p_{o,K} - \sum_{E'\in\partial K} \beta_{K,E,E'} t p_{o,K,E'} + \gamma_{K,E}, \quad E \in \partial K, \quad \ldots\ldots\ldots\ldots\ldots (18)$$

with $\theta_{K,E}$ and $\beta_{K,E,E'}$ given in Appendix A and the capillary pressures included in $\gamma_{K,E}$:

$$\gamma_{K,E} = q^{\mathrm{g}}_{K,E} \sum_\alpha \mathrm{k}_{\alpha,K}\rho_{\alpha,K} + q^c_{wo,K,E} - q^c_{go,K,E}. \quad \ldots\ldots\ldots (19)$$

The computation of $q^c_{wo,K,E}$ and $q^c_{go,K,E}$ will be discussed in the next subsection.

The MHFE discretization of the pressure equation proceeds along the same lines. First, the phase fluxes are eliminated in favor of the total flux expression, with Eq. 12. Then Eq. 9 is multiplied by $\boldsymbol{w}_{K,E}$ and integrated over each element. The time derivative is discretized by the implicit backward Euler scheme with timestep Δt. After algebraic manipulations, the final form of the MHFE approximation to the pressure equation is

$$p^{n+1}_{o,K} = \frac{\Delta t}{\tilde{\alpha}_K \Delta t + \kappa_T \phi |K|} \left[\frac{\kappa_T \phi |K|}{\Delta t} p^n_{o,K} + \sum_{E\in K} \tilde{\beta}_{K,E} p^{n+1}_{o,K,E} + \tilde{\gamma}_K + \sum_i \bar{\mathrm{v}}_i \left(F_{i,K} - \sum_E \sum_\alpha q^{\mathrm{diff}}_{i,\alpha,K,E} \right) \right]. \quad \ldots\ldots\ldots\ldots\ldots (20)$$

The coefficients are given in Appendix A and are evaluated at the nth timestep.

A global matrix system for the pressures and fluxes is obtained by requiring that the total fluxes $q_{K,E}$ and pressure traces $tp_{o,K,E}$ be continuous across edges. The first constraint allows the elimination of $q_{K,E}$ from Eq. 18. For each edge E we collect the terms on the right of Eq. 18 to find a linear system:

$$\mathrm{R}^T \mathbf{P} - \mathrm{M}\mathbf{T}_P = \mathbf{I}, \quad \ldots\ldots\ldots\ldots\ldots\ldots\ldots (21)$$

with the matrices defined in Appendix A. Similarly, we collect the terms in Eq. 20 in a second linear system:

$$\mathrm{D}\mathbf{P} - \tilde{\mathrm{R}}\mathbf{T}_P = \mathbf{G}. \quad \ldots\ldots\ldots\ldots\ldots\ldots\ldots (22)$$

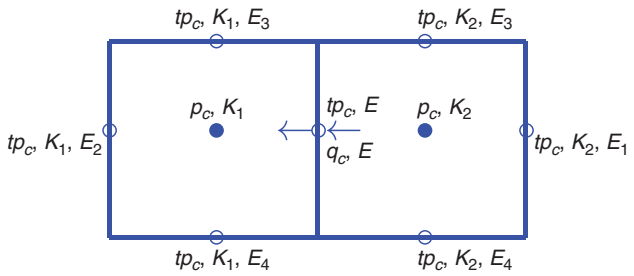

Fig. 1—Element average capillary pressure p_c and capillary pressure traces tp_c, with $tp_{c,K_1,E_1} = tp_{c,K_2,E_2} = tp_{c,E}$ and similarly $q^c_{K_1,E_1} = q^c_{K_2,E_2} = q^c_E$. Either gas/oil or water/oil capillary pressures can be represented by p_c and tp_c. The phase index is dropped for brevity.

The coefficients of the matrices in Eq. 22, provided in Appendix A, show that D is diagonal. This allows the elimination of $\mathbf{P}$ from Eqs. 21 and 22 and finding a linear system for $\mathbf{T}_P$ alone:

$$(\mathrm{M} - \mathrm{R}^T\mathrm{D}^{-1}\tilde{\mathrm{R}})\mathbf{T}_P = \mathrm{R}^T\mathrm{D}^{-1}\mathbf{G} - \mathbf{I}. \quad \ldots\ldots\ldots\ldots (23)$$

In the full algorithm, Eq. 23 is solved first with an off-the-shelf sparse matrix solver (Davis 2004). After finding the pressure traces $\mathbf{T}_P$, the element-averaged pressures are obtained by inexpensive back substitution in Eq. 21, and the total fluxes are found from Eq. 18.

The benefits of the MHFE method are the (1) accuracy of the resulting velocity field, (2) natural incorporation of the permeability tensor and any degree of heterogeneity, (3) straightforward implementation on complex unstructured grids, and (4) an analogues property to the DG discretization—the MHFE method provides not only the element-averaged pressure but also the pressures on the edges.

Discrete Fracture Model. The details of our discrete fracture model for compositional three-phase flow are discussed in Moortgat and Firoozabadi (2012). The basic concept is that fractures, which may have an aperture of $\leq$1 mm, are combined with a small slice (to the magnitude of 10 cm or larger) of the matrix blocks on either side into larger computational elements. The assumption is that a large transverse permeability instantaneously equilibrates the fluid in the fracture with that in the immediate matrix neighborhood. This is a good approximation as long as the width of the aforementioned slices are small compared with the size of the matrix blocks, and the matrix permeability is not too low ($\geq$0.1 md). The computation element, referred to as crossflow-equilibrium (CFE) element, has one saturation, density, and composition for the mixed fracture and matrix fluids. However, the fluxes across the CFE edges take into account the matrix and fracture mobilities and permeabilities. Along the fracture direction, the fluxes are the sum of the matrix and fracture fluxes, integrated over the fracture aperture and cross section of the included matrix slices.

We denote the fracture aperture as Δf, the width of the CFE (perpendicular to the fracture) as E, ϵ as equal to $\Delta f/E$, and superscripts f and m as the fracture and matrix properties, respectively. The total Darcy flux across the edge E can then be written in terms of the normal component of the gradient operator ∇_E and the phase pressures as

$$\begin{aligned} q_{\alpha,K,E} &= \epsilon q^f_{\alpha,K,E} + (1-\epsilon) q^m_{\alpha,K,E} \\ &= -[\epsilon \mathrm{k}^f_\alpha + (1-\epsilon)\mathrm{k}^m_\alpha](\nabla_E p_\alpha - \rho_\alpha q^g_{K,E}) \\ &= -\mathrm{k}^{\mathrm{tot}}_\alpha(\nabla_E p_\alpha - \rho_\alpha q^g_{K,E}). \quad \ldots\ldots\ldots\ldots (24) \end{aligned}$$

In other words, the fluxes across edges that are intersected by a fracture are obtained simply by replacing k_α with the total effective matrix-plus-fracture mobility $\mathrm{k}^{\mathrm{tot}}_\alpha$ in $\theta_{K,E}$, $\beta_{K,E,E'}$, and $\gamma_{K,E}$ in the MHFE discretization (note the different notations of $\mathrm{k}^{\mathrm{tot}}_\alpha$ for the matrix-plus-fracture effective phase mobilities and k_t for the sum of effective phase mobilities). In the direction perpendicular to the fractures, the computation of the fracture-to-matrix flux is avoided by the crossflow equilibrium assumption. The flux across edges between CFE and matrix elements is computed from the matrix permeability and mobility. We emphasize that through Eq. 24 we allow for different relative permeability and capillary pressure relations for the fracture and matrix contributions inside a single CFE element.

Capillary Pressures. The element-averaged capillary pressures $p_{c,go,K}$ and $p_{c,wo,K}$ are computed from the element-averaged saturations $S_{\alpha,K}$. There is no robust theory describing the exact functional dependence in Eqs. 7 and 8, particularly in a three-phase setting. In the numerical examples, we will use capillary pressures of the form (Bentsen and Anli 1976)

$$p_{c,go}(S_o) = \sigma_{go}\sqrt{\frac{\phi}{\mathrm{K}}}\log S_{o,\mathrm{eff}}, \text{ with } S_{o,\mathrm{eff}} = \frac{S_o - S_{wc} - S_{rog}}{1 - S_{wc} - S_{rog} - S_{rg}} \quad \ldots\ldots\ldots\ldots\ldots\ldots (25)$$

$$p_{c,wo}(S_w) = -\sigma_{wo}\sqrt{\frac{\phi}{\mathrm{K}}}\log S_{w,\mathrm{eff}}, \text{ with } S_{w,\mathrm{eff}} = \frac{S_w - S_{wc}}{1 - S_{wc} - s_{row}}, \quad \ldots\ldots\ldots\ldots\ldots\ldots (26)$$

with σ_{go} and σ_{wo} as the gas/oil and water/oil surface tensions, respectively; S_{wc} as the connate or residual water saturations; S_{rog} as the ROS to gas; S_{row} as the ROS to water; and S_{rg} as the residual or critical gas saturation. Alternatively, our simulator allows for tabulated relative permeability and capillary pressure data. For mixed-wet media, the water/oil capillary pressure curve may have a positive part at low water saturations and a negative part at higher water saturations. For such conditions, the behavior changes dramatically as the saturation passes through the zero-point of the capillary pressure curve. We assume a constant water/oil surface tension and gas/oil surface tension that is either constant or computed from the phase compositions, molar densities, and parachors P_i as

$$\sigma_{go}[\text{in N/m}] = 10^{-27}\left[\sum_{i=1}^{n_c} P_i(c_o x_{i,o} - c_g x_{i,g})\right]^4. \quad \ldots\ldots (27)$$

Other functional relationships may be used, such as Brooks and Corey (1964), in which $P_{c,wo} \propto S^{-1/n}_{w,\mathrm{eff}}$. A more sophisticated computation of three-phase capillary pressures and relative permeabilities, including hysteresis effects, was proposed in Hustad and Browning (2010).

A complexity arises from the computation of capillary pressure gradients. Hoteit and Firoozabadi (2008b) propose to use the same MHFE approximation that is used for the oil pressure. Although this approach has desirable features, it involves the CPU-intensive solution of a second global matrix system. To generalize this approach to three-phase flow, we would have to solve three global linear systems, for $tp_{o,K,E}$, $tp_{c,go,K,E}$, and $tp_{c,wo,K,E}$. Instead, we propose a local computation of the capillary pressure gradients from the gradients within each element, together with the constraints of mass conservation (flux continuity) at edges and continuity of the capillary pressure. We emphasize that in multiphase flow and/or in heterogeneous media, the capillary pressure gradient itself is generally not continuous.

We derive the expression for $q^c_{go,K,E}$. The computation of $q^c_{wo,K,E}$ is similar. Consider two neighboring elements K_1 and K_2 with common edge E and average capillary pressures p_{c,go,K_1} and p_{c,go,K_2} and capillary pressure traces $tp_{c,go,K,E}$, as in **Fig. 1.** We require the capillary pressure to be continuous across edges E, such that $tp_{c,go,K_1,E} = tp_{c,go,K_2,E} = tp_{c,go,E}$.

If Δx_{K_1} and Δx_{K_2} are the widths of elements K_1 and K_2, respectively, we can compute $q^c_{go,K,E}$ from the local gradients inside each element as

$$q^c_{go,K_1,E} = -\mathrm{k}_{g,K_1,E}\frac{tp_{c,go,E} - p_{c,go,K_1}}{\Delta x_{K_1}/2} \quad \text{and}$$

$$q^c_{go,K_2,E} = -\mathrm{k}_{g,K_2,E}\frac{p_{c,go,K_2} - tp_{c,go,E}}{\Delta x_{K_2}/2}. \quad \ldots\ldots\ldots\ldots (28)$$

Eq. 28 is for structured grids. In unstructured grids, the expression should be modified with the angles corresponding to the normal component of the flux with respect to edge E, and Δx would refer to the distance to the center of the element. We further require the capillary-driven flux to be continuous, such that $q^c_{go,K_1,E} = -q^c_{go,K_2,E}$ (q is defined with respect to the normal). Note that both the phase mobilities and the absolute permeabilities may be different in neighboring elements, such that the continuity of capillary pressure can be guaranteed only by discontinuous phase saturations at the edge E. From the condition of continuous fluxes, we can solve Eq. 28 for $tp_{c,go,E}$ and substitute the solution back into Eq. 28 to find

$$q^c_{go,K_1,E} = -q^c_{go,K_2,E} = -\|k_{g,\text{eff}}\| \frac{p_{c,go,K_2} - p_{c,go,K_1}}{(\Delta x_{K_1} + \Delta x_{K_2})/2} \quad \ldots . \quad (29)$$

$$\|k_{g,\text{eff}}\| = \frac{(\lambda_{g,K_1,E}\mathrm{K}_{K_1})(\lambda_{g,K_2,E}\mathrm{K}_{K_2})(\Delta x_{K_1} + \Delta x_{K_2})}{\Delta x_{K_1}\lambda_{g,K_1,E}\mathrm{K}_{K_1} + \Delta x_{K_2}\lambda_{g,K_2,E}\mathrm{K}_{K_2}}. \quad \ldots . \quad (30)$$

Note that in Eq. 30, $\|k_{g,\text{eff}}\|$ is the harmonic average of the effective gas mobilities in elements K_1 and K_2. An equivalent expression can be derived for q^c_{wo}. With Eq. 29, we avoid the explicit computation of the capillary pressures on edges. Note that if one uses Eq. 30, there is no capillary-driven flux across an edge E when the gas phase is absent or immobile in K_1 or K_2. This underestimates the effect of capillarity in heterogeneous or fractured media. A more physical approach is to use the upwind value of the gas mobility ($\lambda_{g,K_1,E} = \lambda_{g,K_2,E} = \tilde{\lambda}_{g,E}$) with the harmonic average of the absolute permeability, which also satisfies Eqs. 28–30.

When threshold capillary pressure is significant, the fluxes q^c_{go} and q^c_{wo} may not be continuous, and additional terms have to be added to the preceding equations. In this work, we consider applications with negligible threshold capillary pressures, such as imbibition by water injection into oil.

Upwinding. The most significant complication in incorporating capillarity in the fractional-flow formulation for three-phase flow turns out to be the construction of the phase fluxes from the total flux with Eq. 12. As already discussed, the total flux $\boldsymbol{u}_t$ is continuous across edges by MHFE design. However, from Eq. 12 it is clear that the phase fluxes are continuous only if a unique value of the phase mobilities is assigned to each edge E. One choice could be the average mobility, but this significantly underestimates the flux when a phase is mobile in one element but not in the neighboring element. A second choice could be the upwind mobility with respect to the known total flux $\boldsymbol{u}_t$, but this leads to erroneous and unstable results when there is countercurrent flow caused by gravity or capillarity. The only physically justifiable option is to use the upwind mobilities with respect to the phase fluxes. Unfortunately, the phase fluxes may change rapidly enough that even the directions cannot be reliably obtained from results at the previous timestep. A rigorous approach requires upwind mobilities with respect to the phase fluxes at the current timestep.

Determining even the sign of the phase fluxes before the upwind mobilities are known is a challenge. The gravity and capillary terms in Eq. 12 may have either sign and are of unknown magnitude when the mobility is not known. In the absence of capillarity, we devised a scheme on the basis of the known phase densities, which determine which phase flux has the same sign as $\boldsymbol{u}_t$ (Moortgat et al. 2011). For the other two phases, we try both combinations of mobilities and select the self-consistent solution. Here, we generalize this method to include capillarity. We define the potential differences as

$$\Phi_{go} = p_{c,go} + (\rho_o - \rho_g)gz \quad \ldots . \quad (31)$$

$$\Phi_{wo} = p_{c,wo} + (\rho_w - \rho_o)gz \quad \ldots . \quad (32)$$

$$\Phi_{wg} = p_{c,wg} + (\rho_g - \rho_w)gz = -(\Phi_{go} + \Phi_{wo}), \quad \ldots . \quad (33)$$

and further simplify the notation by defining the unit vector $\boldsymbol{I} = [1, 1, 1]^T$ and

$$\mathbf{q}^r = \begin{pmatrix} q_g/\tilde{f}^{\text{tot}}_g \\ q_o/\tilde{f}^{\text{tot}}_o \\ q_w/\tilde{f}^{\text{tot}}_w \end{pmatrix}, \quad \boldsymbol{\Phi} = \begin{pmatrix} \Phi_{go} \\ \Phi_{wo} \\ \Phi_{wg} \end{pmatrix}, \quad \tilde{\mathrm{k}}^{\text{tot}} = \begin{pmatrix} \tilde{\mathrm{k}}^{\text{tot}}_g \\ \tilde{\mathrm{k}}^{\text{tot}}_o \\ \mathrm{k}^{\text{tot}}_w \end{pmatrix}, \quad \ldots . \quad (34)$$

with the understanding that $q_\alpha = 0$ when $\tilde{f}^{\text{tot}}_\alpha = 0$ (this definition is purely for notational convenience). The effective mobilities $\tilde{\mathrm{k}}^{\text{tot}}_\alpha$ and fractional-flow functions $\tilde{f}^{\text{tot}}_\alpha = \tilde{\mathrm{k}}^{\text{tot}}_\alpha / \sum_\alpha \tilde{\mathrm{k}}^{\text{tot}}_\alpha$ may include both matrix and fracture contributions, as in Eq. 24. The fractional-flow functions are incorporated in the left side of the equation because we are interested in finding the direction (sign) of the phase fluxes, which does not depend on the overall fractional-flow factor. $\tilde{f}^{\text{tot}}_\alpha$ is evaluated after all upwind directions have been determined.

With these definitions, Eq. 12 can be written succinctly in vector or matrix notation (with $\otimes$ the outer product) as

$$\mathbf{q}^r = q_t\mathbf{I} - \tilde{\mathrm{k}}^{\text{tot}} \otimes \nabla\Phi = q_t\mathbf{I} + \Psi\tilde{\mathrm{k}}^{\text{tot}}, \quad \text{with}$$
$$\Psi = \begin{pmatrix} 0 & -\nabla\Phi_{go} & \nabla\Phi_{wg} \\ \nabla\Phi_{go} & 0 & -\nabla\Phi_{wo} \\ -\nabla\Phi_{wg} & \nabla\Phi_{wo} & 0 \end{pmatrix}. \quad \ldots . \quad (35)$$

The full upwinding algorithm proceeds in the following steps for an element K with neighboring element K':

1. From Eq. 35, we can determine the sign of the flux of one of the phases a priori, irrespective of the unknown $\tilde{\mathrm{k}}^{\text{tot}}_\alpha$. Specifically, we first find the phase flux parallel ($\|$) to the total flux and label this phase by α_1. If $q_t > 0$, then
   - If $\Phi_{go} \le 0$ and $\Phi_{wg} \ge 0$, then $q_g \| q_t (\forall \Phi_{wo})$
   - If $\Phi_{go} \ge 0$ and $\Phi_{wo} \le 0$, then $q_o \| q_t (\forall \Phi_{wg})$
   - If $\Phi_{wo} \ge 0$ and $\Phi_{wg} \le 0$, then $q_w \| q_t (\forall \Phi_{go})$,

   and similarly for $q_t < 0$ (note that because of Eq. 33, this covers all possible combinations of signs for Φ_{go}, Φ_{wo}, and Φ_{wg}). Because $q_{\alpha_1} \| q_t$, we know the upwind mobility: $\tilde{\mathrm{k}}^{\text{tot}}_{\alpha_1} = \mathrm{k}^{\text{tot}}_{K,\alpha_1}$, if $q_t \ge 0$, and $\tilde{\mathrm{k}}^{\text{tot}}_{\alpha_1} = \tilde{\mathrm{k}}^{\text{tot}}_{K\prime,\alpha_1}$, for $q_t < 0$.
2. If one of the phases is absent or immobile in both K and K', we denote the second mobile phase by α_2 and find the sign of q_{α_2} by evaluating the appropriate relation with Eq. 35, with the $\tilde{\mathrm{k}}^{\text{tot}}_{\alpha_1}$ obtained in Step 1, and skip to Step 8.
3. When all phases are mobile in K or K' (but not necessarily in both), we cannot determine the sign of either of the remaining two phases directly. In this case, we pick either choice of upwind mobility, i.e., we choose either $\tilde{\mathrm{k}}^{\text{tot}}_{\alpha_2} = \mathrm{k}^{\text{tot}}_{K,\alpha_2}$ or $\tilde{\mathrm{k}}^{\text{tot}}_{\alpha_2} = \mathrm{k}^{\text{tot}}_{K\prime,\alpha_2}$. In the next steps, we verify whether the resulting signs of the phase fluxes are consistent with this choice of upwind mobility. If they are not, we return to this step and choose the opposite choice for the upwind direction of $\tilde{\mathrm{k}}^{\text{tot}}_{\alpha_2}$.
4. With $\tilde{\mathrm{k}}^{\text{tot}}_{\alpha_2}$ from Step 3 and $\tilde{\mathrm{k}}^{\text{tot}}_{\alpha_1}$ from Step 1, compute the sign of the third phase flux q_{α_3}.
5. From the sign of q_{α_3} determine the upwind value for $\tilde{\mathrm{k}}^{\text{tot}}_{\alpha_3}$.
6. With $\tilde{\mathrm{k}}^{\text{tot}}_{\alpha_1}$ from Step 1 and $\tilde{\mathrm{k}}^{\text{tot}}_{\alpha_3}$ from Step 5, determine the sign of phase flux q_{α_2}.
7. If the sign of q_{α_2} is consistent with the selection in Step 3, we proceed to Step 8. If the sign is inconsistent (i.e., we selected $\tilde{\mathrm{k}}^{\text{tot}}_{\alpha_2} = \mathrm{k}^{\text{tot}}_{K,\alpha_2}$ but $q_{\alpha_2} < 0$, or we chose $\tilde{\mathrm{k}}^{\text{tot}}_{\alpha_2} = \mathrm{k}^{\text{tot}}_{K\prime,\alpha_2}$ but $q_{\alpha_2} \ge 0$), we choose the second option in Step 3 and repeat Steps 4 through 6.
8. With all upwind $\tilde{\mathrm{k}}^{\text{tot}}_\alpha$ known, compute $\tilde{f}^{\text{tot}}_\alpha$ and, finally, the phase fluxes q_α.

We note that (capillary) pressure gradients may be strongly discontinuous across grid-cell edges, particularly in heterogeneous and fractured domains. There may be an issue with computing the phase fluxes directly from Darcy's law by finite differencing, and determining the upwind phase mobilities from the difference in phase potentials ($p_\alpha + \rho_\alpha gz$) between elements K and K'. As the

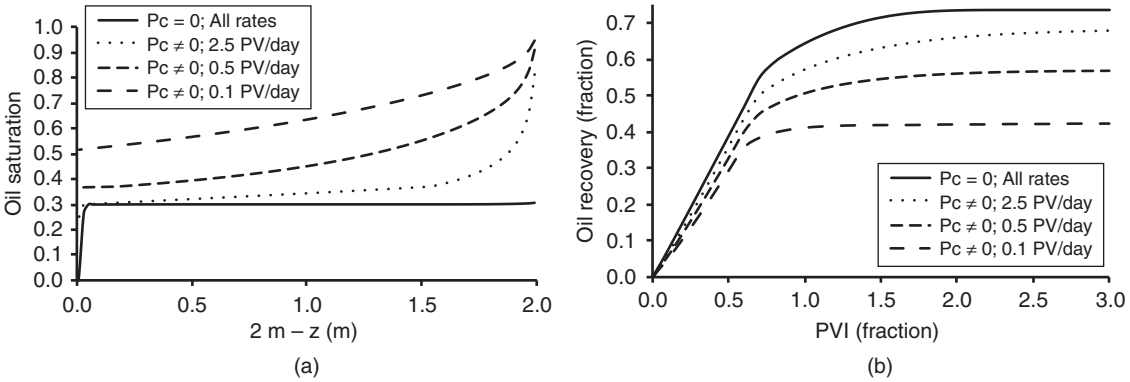

Fig. 2—Example 1: Capillary end effect for drainage. A nonwetting gas phase (C_1) is injected in the top of a 30 × 200-cm domain saturated with a wetting oil phase (n-C_{10}). Steady-state oil saturations at 3 PVI (a) and oil recoveries (b).

simplest example, the phase potential in K may be higher than in K', but not result in flow of the phase from K to K' if the gradient of the potential inside K is zero. Similarly, the average potential may be the same in both elements, but the potential gradient may be nonzero on either side of the edge. In the MHFE fractional-flow formalism proposed here, we first compute a vector field for the total flux that is continuous at every point in the domain. The method provides both a continuous pressure and continuous flux at each edge, which in turn determines the continuous phase fluxes through the procedure described previously. This feature makes the MHFE approach particularly attractive for heterogeneous and fractured porous media.

CFL Condition. The explicit mass-transport update incurs a CFL constraint on the timestep (Courant et al. 1928) in guaranteeing numerical stability. In single-phase and immiscible multiphase flow, this is a motivation to use fully implicit methods, which may be unconditionally stable. However, for multicomponent multiphase flow, the linear system that has to be solved in a fully implicit method becomes very expensive and poses additional complications with phase-stability analysis and accurate initial guesses to perform the phase-split computations (Moortgat et al. 2012). For these and other reasons, the IMPEC approach appears to be favored for compositional multiphase flow.

In our model, we include convective, diffusive, and capillary fluxes, each of which carries its own constraint on the timestep. Although the CFL condition for the convective flux is linear in the mesh size, the diffusive and capillary fluxes require more-severe timestep limits, quadratic in the mesh size. This applies to both lower-order FD and finite-volume methods and to higher-order methods. However, the higher-order methods allow considerably coarser mesh sizes, which alleviate the CFL condition. The CFL limits on the convective and diffusive fluxes are discussed in Moortgat and Firoozabadi (2012). For the capillary flux, a CFL condition is given in Coats (2003). The overall timestep is set by the minimum of the convective, diffusive, and capillary CFL conditions. We note that the CFL condition is a sufficient, but not necessary, condition for numerical stability. An alternative approach is to adopt an adaptive timestep selection scheme on the basis of fluctuations in pressure and other variables, as in Hoteit and Firoozabadi (2008b). This may allow for larger timesteps and is commonly used in commercial simulators. In large-scale fractured reservoirs, we find that the CFL condition is generally determined by the convective flow through the fractures.

Numerical Experiments

We present six numerical examples to verify our model by comparing with the work of others and by investigating known features of capillarity: (1) the capillary end effect for two-phase gas/oil flow in both core- and large-scale domains; (2) the effects of permeability discontinuities perpendicular to the flow; (3) gas and water injection in a large-scale oil-saturated domain with layers parallel to the flow, in which we compare with results for a similar example in Hoteit and Firoozabadi (2008b) for incompressible two-phase flow; (4) capillary water imbibition in a fractured core; (5) drainage through depletion from large-scale fractured domains; and (6) depletion, water imbibition, and CO_2 injection in a fractured domain. To provide easily reproducible examples that clearly highlight important aspects of capillarity, we neglect Fickian diffusion and consider fluids that do not exhibit strong phase-behavior effects. Reinfiltration caused by gravity and capillarity are automatically taken into account in fractured media.

The computations are carried out on a 2.8-GHz quad-core Core i7 processor with 12-GB RAM. The code is parallelized, but for easier comparison, we report CPU times for serial runs.

Example 1: Capillary End Effect. It is well known that capillarity causes an impediment to flow at the outlet, because of the steep capillary pressure gradient at the producing boundary [e.g., Huang and Honarpour (1998)]. As a result, the saturation near the outlet may remain close to the initial value. How far into the domain this effect extends depends on the injection rate. Injection at a high rate can more effectively counter the capillary end effect. In this example, we study the end effect for drainage of an oil-saturated core by injection of a nonwetting gas phase. Specifically, we model methane (C_1) injection into a vertical core saturated with normal decane (n-C_{10}) at a temperature of 310 K and initial (bottom) pressure of 100 bar. At this condition, evaporation of n-C_{10} into the C_1 gas phase is low. The core dimensions are 30 × 200 cm, discretized by 3 × 200 elements (for essentially 1D displacement). C_1 is injected uniformly from the top boundary, and production is from the bottom at constant pressure. The capillary pressure, in terms of surface tension $\sigma_{go} = 5$ dyne/cm, is given by Eq. 25 with porosity $\phi = 20\%$ and permeability $K = 10$ md. We assume linear relative permeabilities, no connate water, and an ROS to gas of 30%. At the given condition, the viscosity ratio between C_1 and n-C_{10} is 18, which results in early breakthrough and requires many pore volumes (PV) to recover the mobile oil, even without capillarity. To speed up the computation, we assume (artificial) relative permeability endpoints of unity for oil and 0.27 for gas, such that the mobility ratio is λ_g/λ_o is approximately 5.

We consider three injection rates: 0.1, 0.5 and 2.5 PV/D. Injection is continued for 3 PV, such that the saturation in the core reaches a steady state. We compare with a simulation in which capillarity is neglected (which is independent of injection rate). The CPU times are <1 minute without capillarity and 1, 4, and 9 minutes for the simulations with capillarity for the three injection rates, respectively.

Fig. 2a shows the steady-state oil saturation and Fig. 2b the oil recovery for all four simulations (the horizontal axis has the injector on the left and the producer on the right). Without capillarity, oil is recovered down to the ROS (and an additional small amount near the injection well caused by evaporation by the many local PV of C_1 that passed through those elements). When capillarity is accounted for, a considerable amount of oil is stranded. At the

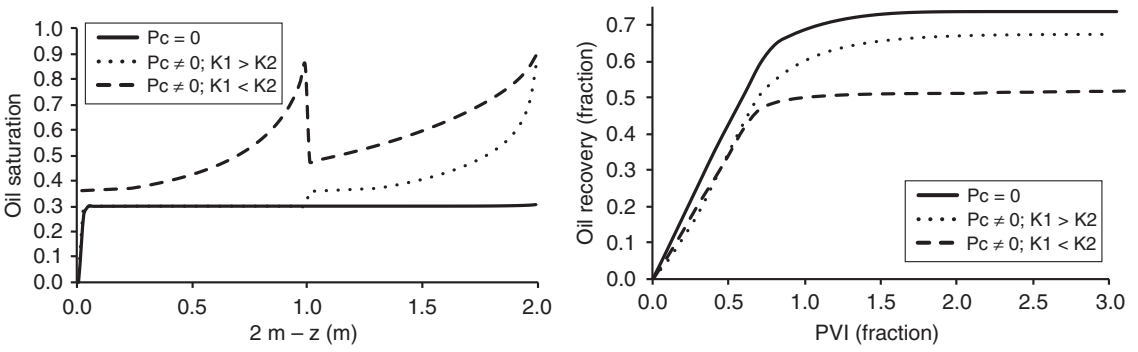

Fig. 3—Example 2: Capillary effect on drainage in two-layer core. A nonwetting gas phase (C_1) is injected in the top of a 30 × 200-cm domain saturated with a wetting oil phase (n-C_{10}). Steady-state oil saturations at 3 PVI (a) and oil recoveries (b).

highest injection rate, the end effect mainly affects the wetting-phase saturation near the production side. At lower rates, however, capillarity considerably reduces flow of oil throughout the domain and the final recovery is only half of the nonresidual oil. These results are similar to the findings in Huang and Honarpour (1998) for oil displacing water. In large-scale applications, the importance of the capillary end effect is not significant.

Example 2: Gas/Oil Flow Perpendicular to Permeability Discontinuities. The effect of capillarity is most pronounced in heterogeneous media, because of discontinuities in permeability, saturation, and capillary pressure gradients. We extend the previous example to layered media with all parameters the same, except for the permeability. The injection rate is 0.5 PV/D. First, we consider two layers of 100 md and 1 md and the effect of the layer order. We denote the permeability in the top layer (1 m $< z <$ 2 m) by K_1 and the permeability in the bottom layer (0 m $< z <$ 1 m) by K_2 and consider both $K_1 > K_2$ and $K_1 < K_2$. The relation in Eq. 25 implies that continuity of the capillary pressure requires $S_{o,2} = S_{o,1}^{\sqrt{K_2/K_1}}$ at the interface.

Fig. 3a shows the steady-state oil saturation at 3 PV injected (PVI) and Fig. 3b the oil recovery for both configurations with and without capillarity. Without capillarity, the result is the same for both configurations and the same as for injection into a homogeneous core with a harmonically averaged permeability (i.e., as in the preceding example). The differences are pronounced when capillarity is accounted for. For the configuration in which the first layer has the high permeability (CPU time is 3 minutes), all mobile oil is recovered from the top layer, but some oil remains in the low permeability bottom layer because of the end effect. The oil recovery in this case is close to that without capillarity (CPU is <1 minute). When the top layer has a low-permeability (CPU time is 8 minutes), a large amount of oil is trapped in both layers because of the capillary pressure gradient at the interface, and recovery is significantly reduced. These findings agree well with the results presented in Corrêa and Firoozabadi (1996).

Next, we consider 10 alternating layers, with the same permeabilities as previously discussed, starting from the bottom with a high-permeability layer. **Fig. 4** illustrates that for multiple layers, oil is recovered efficiently from the high-permeability layers, but remains trapped in the low-permeability layers (CPU time is 7 minutes with capillarity). The sharp kink in the oil-recovery plot indicates the early time at which the high-permeability layers have been drained.

This effect applies to larger-scale domains as well, as illustrated in **Fig. 5,** in which the simulation is repeated for a 30 × 200-m domain, with an injection rate of 0.05 PV/yr (CPU time is 1 hour).

Example 3: Water/Oil and Gas/Oil Flow Parallel to Permeability Discontinuities. We compare our simulation results with Example 3a in Hoteit and Firoozabadi (2008b), which considers immiscible and incompressible water injection in a horizontal 500 × 270-m layered domain, discretized by 50 × 90 rectangular elements. The domain has 9 layers with alternating permeabilities of 100 md (starting from the bottom layer) and 1 md. The porosity is 20% in all layers, the injection rate is 11% PV/yr, all residual saturations are zero, and the relative permeabilities are quadratic with unit endpoints. The initial pressure is 300 bar, the temperature is 288 K, and we choose n-C_{10} as the nonwetting phase. At this condition, the water viscosity and density are 1.14 cp and 1.0 g/cm^3, respectively, and the oil viscosity and density are 0.34 cp and 0.74 g/cm^3. We perform compositional simulations with fluid compressibility and assume the same logarithmic dependence of the capillary pressure on water saturation as in Hoteit and Firoozabadi (2008b).

The wetting aqueous phase is injected uniformly from the left boundary, displacing the nonwetting oil phase to the right.

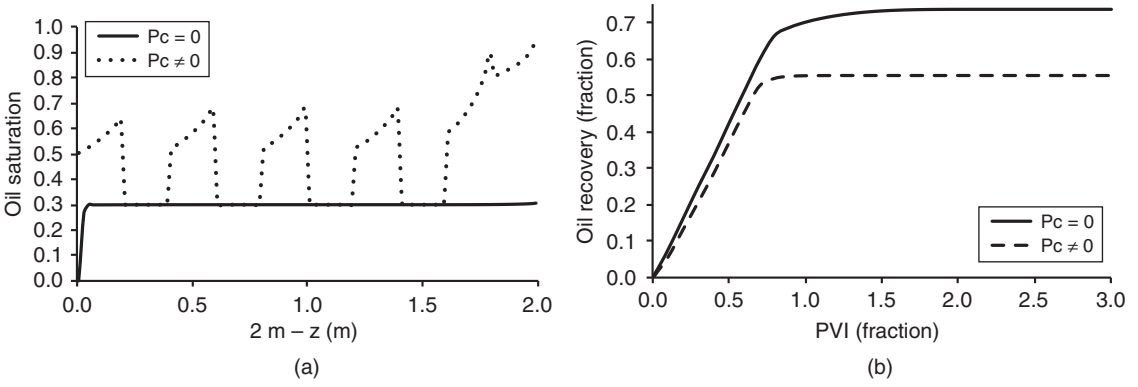

Fig. 4—Example 2: Capillary effect on drainage in 10-layer core. A nonwetting gas phase (C_1) is injected in the top of a 30 × 200-cm domain saturated with a wetting oil phase (n-C_{10}). Steady-state oil saturations at 3 PVI (a) and oil recoveries (b).

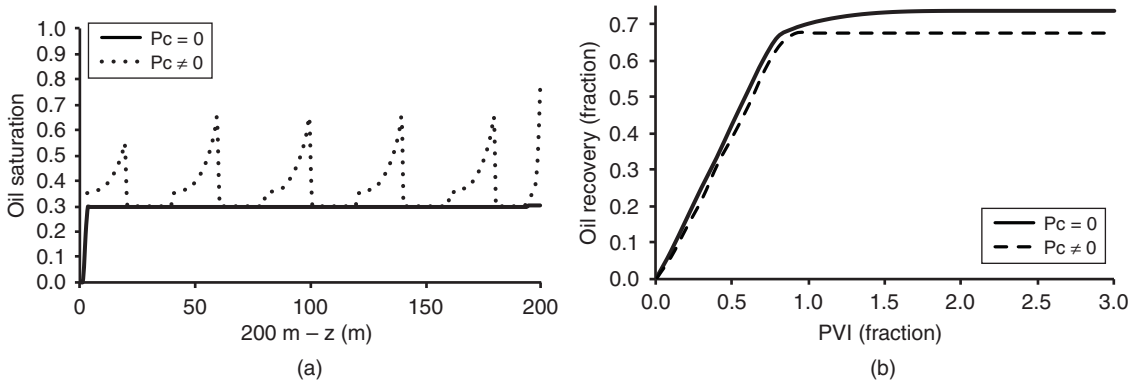

Fig. 5—Example 2: Capillary effect on drainage in 10-layer domain. A nonwetting gas phase (C_1) is injected in the top of a 30 × 200-m domain saturated with a wetting oil-phase (n-C_{10}). Steady-state oil saturations at 3 PVI (a) and oil recoveries (b).

Production is at constant pressure from five wells in the high-permeability layers on the right boundary. **Fig. 6** shows the water saturation at 0.5 PVI, with (CPU time is 30 minutes) and without (CPU time is 3 minutes) capillarity. When capillarity is neglected, water flows predominantly through the high-permeability layers, and breakthrough occurs at approximately 0.55 PVI. The steep contrast in saturation between the high- and low-permeability layers, however, drives considerable crossflow when capillarity is accounted for (Yokoyama and Lake 1981), and we observe a nearly uniform displacement. The results are in excellent agreement with Hoteit and Firoozabadi (2008b), despite small differences in fluid parameters and different modeling approaches. We see the same transverse flow in Fig. 6 in the thin regions around the permeability discontinuities, as reported in Hoteit and Firoozabadi (2008b).

Next, we generalize the problem to the more complicated case with gravity, and considering both strongly water-wet capillary pressures, which are positive for all water saturations, and a mixed-wet curve, which is negative at high water saturations. The modeling of imbibition under mixed-wet conditions is the most challenging problem because of the steeper gradients in capillary pressure as a function of saturation. **Fig. 7** shows the water saturation at 0.5 PVI for simulations without capillarity (Fig. 7a; CPU time is 1 minute), with the same strongly water-wet capillary pressure used in Fig. 6b (Fig. 7b; CPU time is 19 minutes), and for the mixed-wet case (Fig. 7c; CPU time is 3 hours). The capillary pressure curves are given in Fig. 7d for $K = 100$ md. Because of the relatively high injection rate and low effective vertical permeability, there is no significant crossflow between the layers from gravity. The saturation profile for the water-wet case is similar to that without gravity. The more interesting observation is the sweep for the mixed-wet case, which is in between the results without capillarity and with water-wet capillarity. The reason is that at low water saturations, the capillary pressure curves for the water-wet and mixed-wet cases are similar, and capillarity drives crossflow between the layers. However, at high saturations, the capillary pressure gradients across the layer interfaces change sign and oppose further crossflow.

For gas/oil drainage, capillary pressure always opposes crossflow between layers. We carried out simulations for gas injection in the same setup as previously discussed, and the results (not shown) are similar with and without capillarity.

Example 4: Water Injection in Fractured Stacked Blocks. We consider water injection in a fractured domain composed of stacked blocks, saturated with a light oil. The initial oil composition and EOS parameters are given in **Table 1.** The initial pressure is 300 bar, and the temperature is 400 K. The domain is 2 × 10 m and consists of four matrix blocks separated by four discrete fractures, as illustrated in **Fig. 8.** The matrix permeability and porosity are 4 md and 44%, respectively. The fractures have an aperture of 5 mm and the CFE computational fracture elements have a width of 5 cm. The fractures have residual oil and water saturations of 10% and linear relative permeabilities with unit endpoints. In the matrix, the ROS to water is 50%, the endpoint relative permeabilities are $k^0_{row} = 0.3$ and $k^0_{rw} = 1$, and the exponents are $n_w = n_{ow} = 3$. The water-wet capillary pressure is of the form in Eq. 26 with $\sigma_{wo} = 50$ dyne/cm.

We consider the effect of various parameters on oil recovery. The simulations are carried out on 9 × 55-element (Mesh 1) and 19 × 103-element (Mesh 2) grids to check convergence, and both with and without accounting for the capillary pressure. Three PV of water are injected either from the bottom or the top fracture at constant rates of either 8 PV/yr or 80 PV/yr, and production is from the fracture on the other end at a constant pressure. Finally, we consider the impact of fracture permeability by considering first $K^f = 4$ darcies and then $K^f = 100$ darcies. The oil recovery from all simulations with water injection from the bottom is given in **Fig. 9,** and for injection from the top in **Fig. 10.** Next, we will discuss the results in more detail.

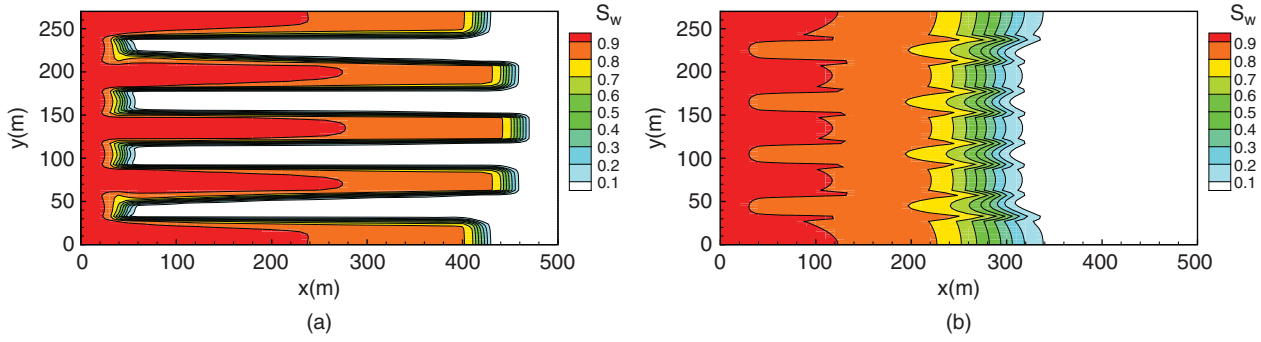

Fig. 6—Example 3: Compressible water injection in oil-saturated layered system without gravity. Water saturation at 0.5 PVI, without capillarity (a) and with strongly water-wet capillary pressure (b).

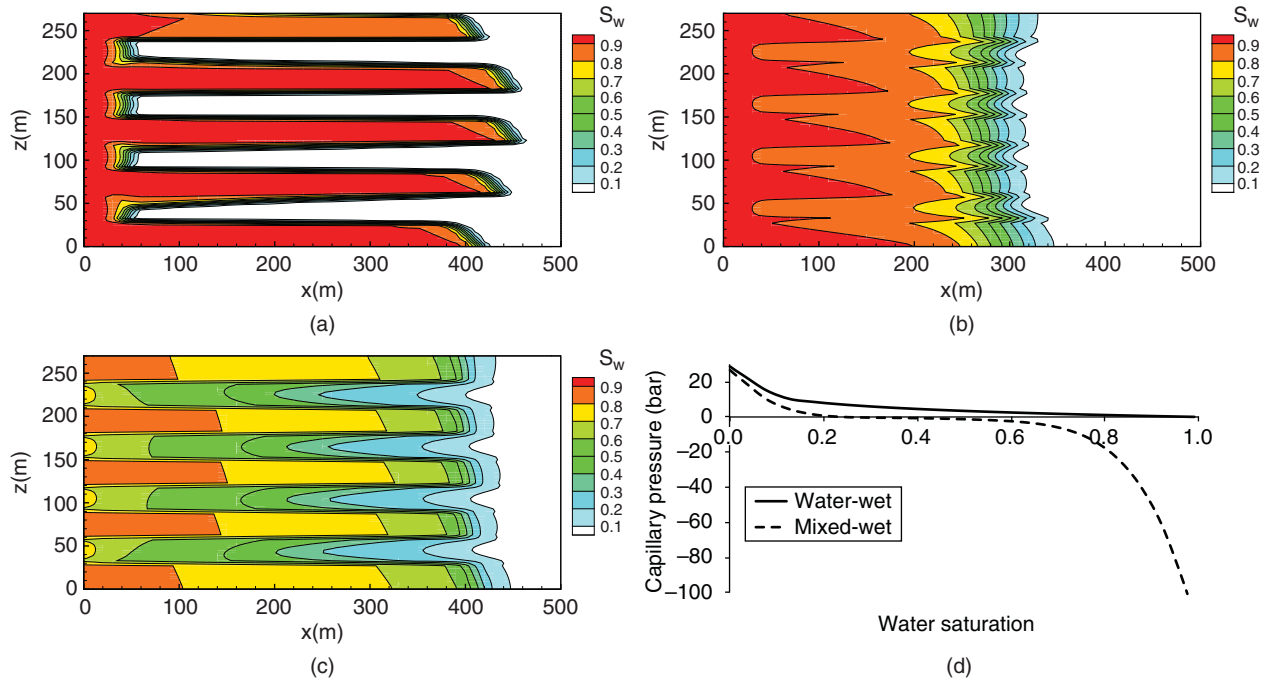

Fig. 7—Example 3: Compressible water injection in oil-saturated layered system with gravity. Water saturation at 0.5 PVI, without capillarity (a), with strongly water-wet capillary pressure (b), and with mixed-wet capillary pressure (c). The capillary pressure curves are given in (d).

The oil-recovery curves in Figs. 9 and 10 serve to illustrate a few key points. First, oil recovery is improved considerably by capillarity during imbibition in fractured media by driving crossflow between the high-permeability fractures and low-permeability matrix, similar to the layered media discussed previously. Inside the matrix blocks, capillarity drives flow from high to low water saturations. Without the capillary-driven crossflow, gravity is the main driver of flow between fracture and matrix blocks. This process, however, is relatively slow and inefficient at high fracture permeability. This is apparent from **Fig. 11,** which shows the water saturation on the fine grid after injecting 0.3 and 1 PV from the bottom fracture with $K^f = 4$ darcies and $K^f = 100$ darcies.

The effect of capillary-driven crossflow is illustrated in **Fig. 12,** which shows the water saturation on Mesh 2 after injecting 0.3 PV for both the low and high injection rates and both fracture permeabilities. We find that at the lower injection rate and fracture permeability, the flow in the matrix is actually faster than in the fracture and the sweep is highly efficient. This translates into the early recovery of nearly all mobile oil (Fig. 9b). Importantly, the results are nearly identical for fracture permeabilities from 4 to 100 darcies. Also beneficial is that, unlike gravitational drainage, the crossflow does not depend on the orientation of the fractures or the direction of flow in the fractures. Specifically, the oil recovery is equally efficient for injection from the bottom or top, as shown in **Fig. 13** and Fig. 10b. The main dependence is on the injection rate. At high rates, there is less time for the crossflow to operate and the oil recovery is reduced. Conversely, without capillarity, injection from the top is even less efficient because gravitational drainage is less effective (Fig. 10a).

Finally, we find that most of the results have converged even on the coarse 9×55 Mesh 1. For the simulations at the low fracture permeability, breakthrough occurs slightly earlier on the coarse grid because of some numerical dispersion, but the final oil recovery is the same. For all other simulations, the results are indistinguishable on Mesh 1 and Mesh 2. The CPU times are nearly the same for simulations with and without capillarity because the CFL condition is determined by the convective flow in the fractures (CFE elements). On Mesh 1, the CPU times for simulations with and without capillarity are approximately 5 minutes, and on Mesh 2 the CPU times are approximately 25 minutes.

Example 5: Gravity Drainage of Fracture Domain. We consider the impact of capillarity on gravity drainage of a fractured domain. The domain is saturated with a light oil with composition and EOS parameters provided in **Table 2.** The temperature is 400 K and the initial pressure at the bottom is 350 bar, which is just above the saturation pressure of 341 bar.

TABLE 1—INITIAL COMPOSITIONS AND EOS PARAMETERS FOR ALL COMPONENTS IN EXAMPLE 4

Species	Composition, n (mol%)	Acentric Factor, ω	Critical Temperature, T_c (K)	Critical Pressure, P_c (bar)	Molar Weight, M_w (g/mol)	Critical Volume, V_c (cm^3/g)	Volume Shift Parameter, VSP	Nonzero Binary Interaction Coefficients With Respect to $C_1 + N_2$, $k_{C_1+N_2,j}$
H_2O	0.00	0.344	647	221	18	2.14	—	—
$C_1 + N_2$	0.45	0.011	190	46	16	6.14	–0.154	—
$C_2 - C_3$	0.12	0.118	328	47	35	4.73	–0.095	0.037
$C_4 - C_6$	0.07	0.234	458	34	70	4.32	–0.047	0.040
$C_7 - C_9$	0.08	0.370	566	26	108	4.24	0.038	0.047
$C_{10} - C_{15}$	0.12	0.595	651	19	166	4.31	0.115	0.056
C_{16+}	0.16	1.427	824	10	386	3.75	0.277	0.072

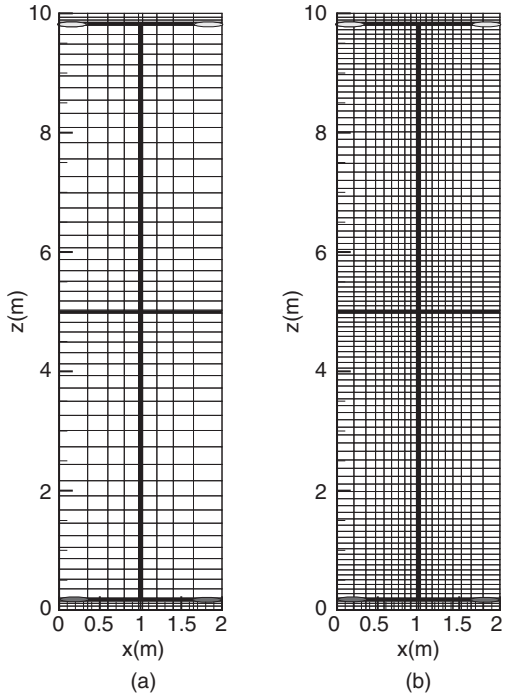

Fig. 8—Example 4: Mesh 1 (a) and Mesh 2 (b) and location of fractures, injection wells, and production wells.

Example 5a: Sugar-cube Fracture Configuration. We first consider a 50×50 m domain, with a sugar-cube-type configuration with 5×5 m matrix blocks. The grid, fractures, and well are shown in **Fig. 14.** The matrix blocks have a porosity of 20%, permeability of 1 md, and are discretized by 36 elements each (the mesh has 71×71 elements). The fractures have a permeability of 100 darcies and aperture of 1 mm, whereas the width of the CF fracture elements is 40 cm. The oil-to-water relative permeability has a power of 3 and endpoint of unity; the water relative permeability has a power 2 and endpoint of 0.3. The ROS to water is 30% in the matrix and 10% in the fractures. To emphasize the effect of capillarity, we assume a rather high surface tension of $\sigma_{go} = 10$ dyne/cm.

In the simulations, the domain is depleted from the bottom fracture (at the left boundary) for 10 years at a constant production rate of 0.06 PV/yr until the pressure has dropped to 120 bar. **Figs. 15 and 16** show the gas saturation at 2, 5, and 10 years for a simulation without and with capillarity, respectively. It is clear that capillarity reduces the amount of gravitational segregation to the top of the domain. The detrimental result is earlier breakthrough of liberated gas and a reduction in oil recovery, as shown in **Fig. 17.**

The lower degree of gravitational segregation may appear to run counter to our discussion earlier on gas injection in layered media, in which we observed fast flow of gas through the high-permeability layers and little crossflow between the high- and low-permeability layers. However, the process is different in this case. In the fractures, the capillary pressure is low and the flow in the fractures is similar with or without capillarity. It is in the matrix that the effect of capillarity is pronounced. Gas appears in the matrix blocks as a result of the pressure drop rather than through convective flow. The gradients in gravitational potential drive segregation of gas toward the top and oil to the bottom, but the flow is opposed by gradients in the gas/oil capillary pressure in the opposite direction. As a result, much of the liberated gas remains trapped in the matrix blocks, as can be seen in Fig. 16. For this simulation the CPU time with capillarity (2 hours) is actually lower than without capillarity (2.8 hours) because the convective fluxes are reduced.

Example 5b: Configuration of Discrete Fractures. One of the features of our crossflow equilibrium model is that we can model any configuration of discrete fractures. To provide an example, we consider now a 100×100-m domain with 35 discrete fractures and a relatively fine mesh of 100×100 elements. The mesh and

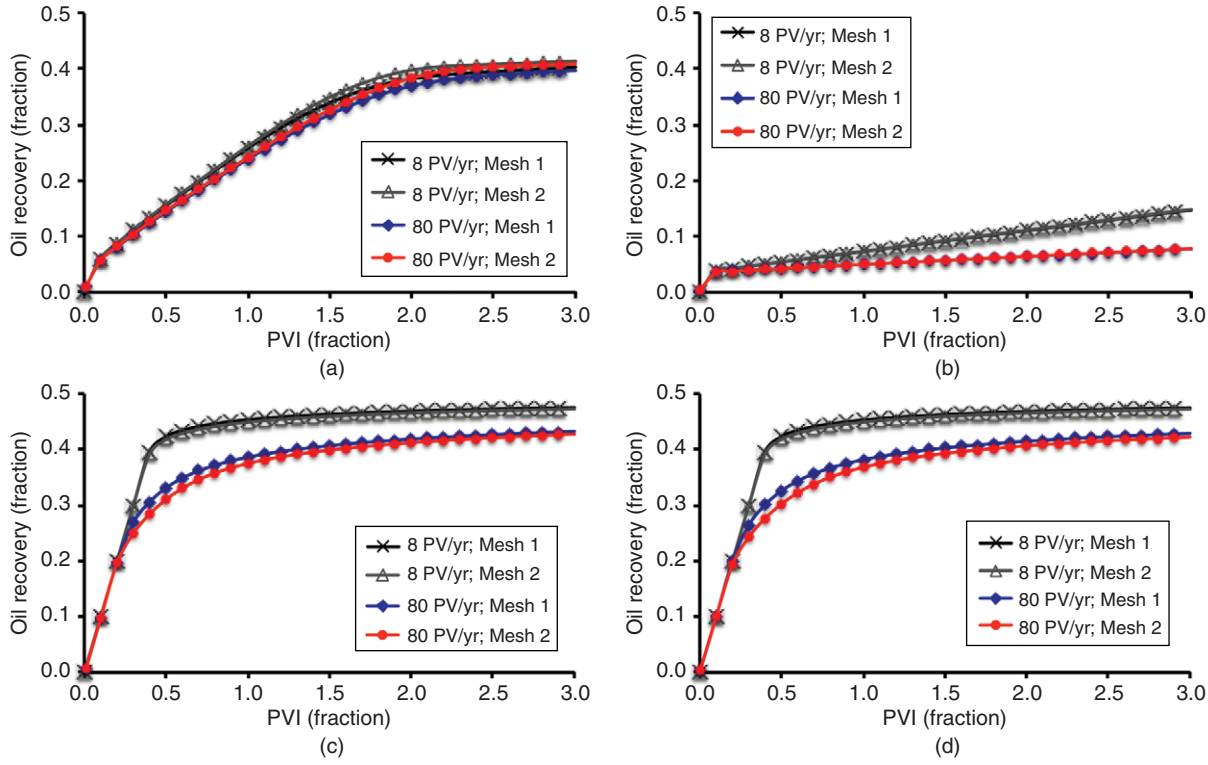

Fig. 9—Example 4: Oil recovery for simulations without capillarity for $K^f = 4$ darcies (a) and $K^f = 100$ darcies (b) and with capillarity for $K^f = 4$ darcies (c) and $K^f = 100$ darcies (d). Results are shown for water injection from the bottom at 8 and 80 PV/yr, and 9×55 (Mesh 1) and 19×103 (Mesh 2) grids.

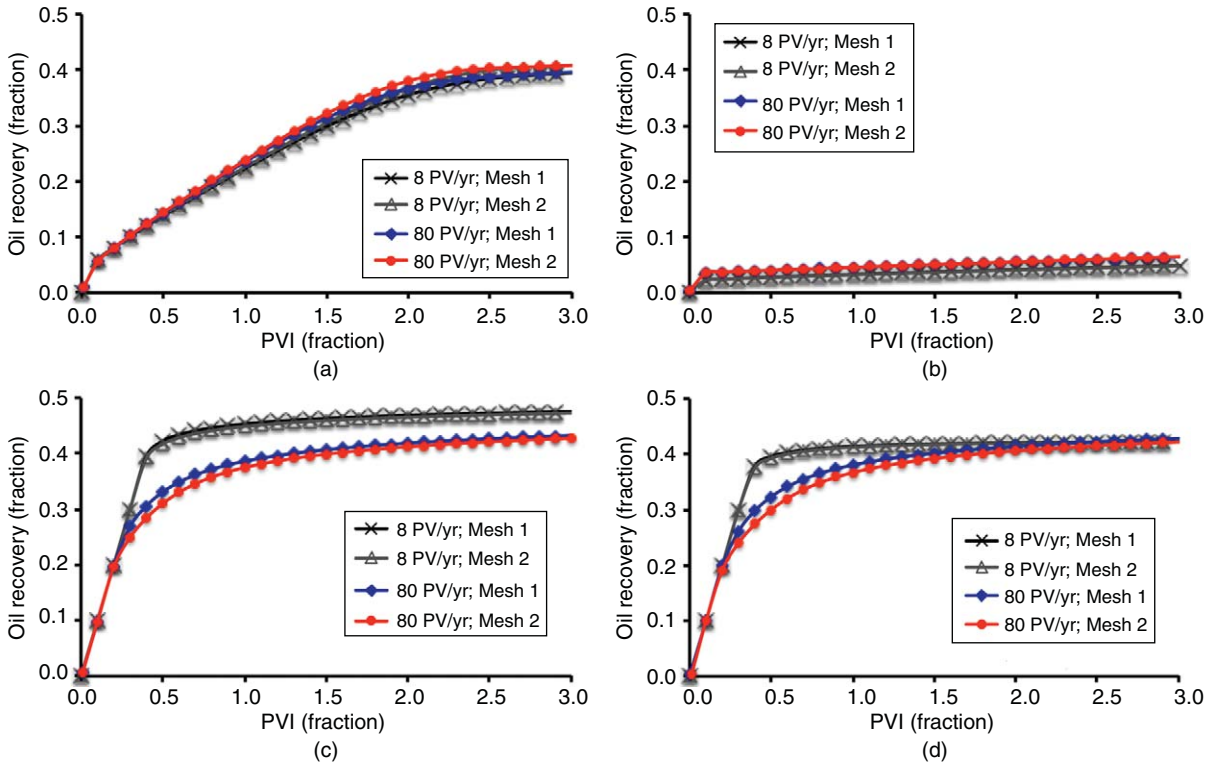

Fig. 10—Example 4: Oil recovery for simulations without capillarity for $K^f = 4$ darcies (a) and $K^f = 100$ darcies (b) and with capillarity for $K^f = 4$ darcies (c) and $K^f = 100$ darcies (d). Results are shown for water injection from the top at 8 and 80 PV/yr, and 9×55 (Mesh 1) and 19×103 (Mesh 2) grids.

the locations of the fractures and the production well (bottom-left corner) are illustrated in **Fig. 18.** All other parameters are the same as previously discussed. Particularly, the production rate is again 0.06 PV/yr, which corresponds to a lower volumetric rate for this larger domain, and results in a more pronounced effect of capillarity.

Figs. 19 and 20 show the gas saturation at 2, 5, and 10 years for simulations without and with capillarity, respectively (CPU of approximately 1 day). We find the same behavior in terms of reduced gravitational segregation and lower oil recovery (**Fig. 21**) because of the capillary pressure gradients. Without capillarity, we further see that when we have discrete fractures that do not span the full height of the domain, much of the gas from the underlying matrix block escapes toward the top through the fractures. We note that the fracture model incorporates all physical interactions between fractures and matrix blocks explicitly, the same as for an unfractured domain. Specifically, reinfiltration from a fracture to neighboring matrix blocks is computed

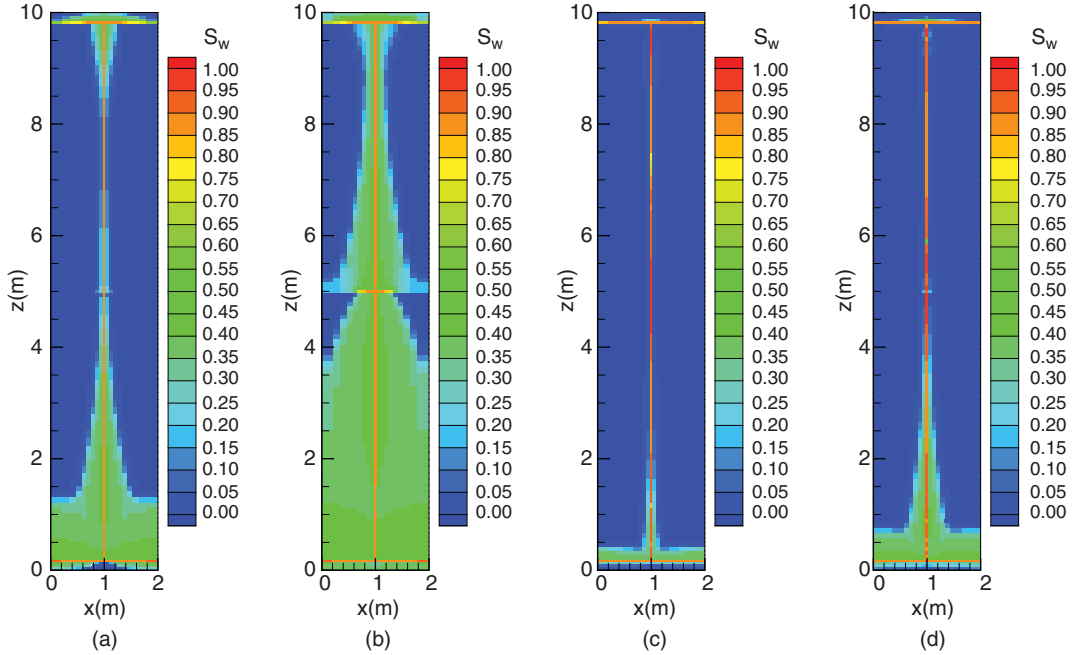

Fig. 11—Example 4: Water saturation at 0.3 PVI (a and c) and 1 PVI (b and d) for simulations without capillarity and with fracture permeability of 4 darcies (a and b) and 100 darcies (c and d). Water is injected at 8 PV/yr from the bottom fracture.

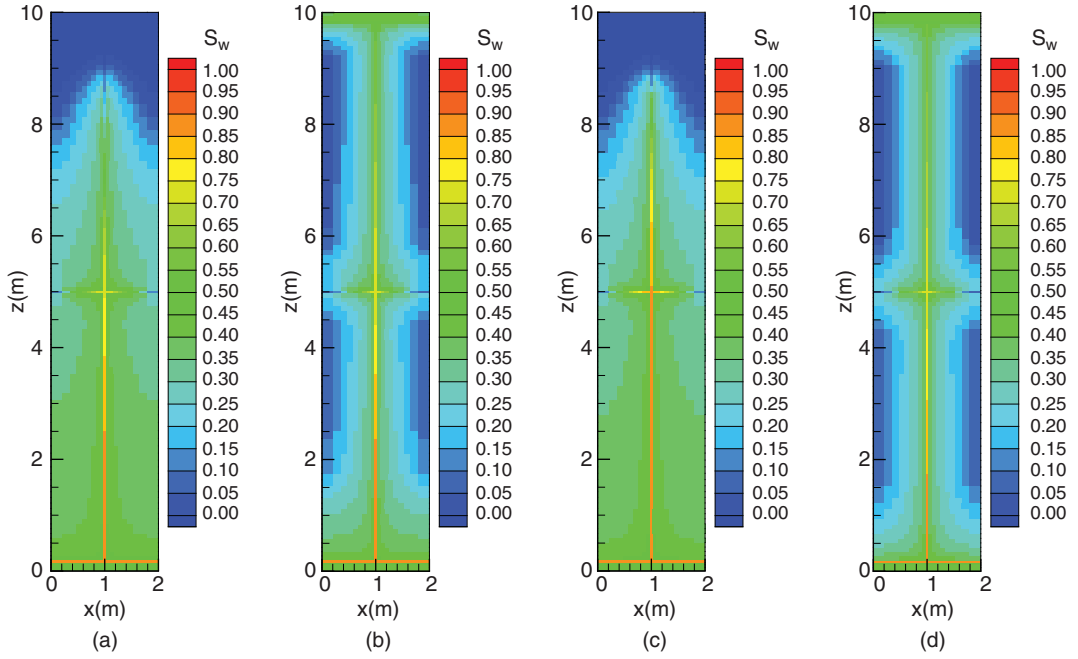

Fig. 12—Example 4: Water saturation at 0.3 PVI for simulations with capillarity and with fracture permeability of 4 darcies (a, b) and 100 darcies (c, d) and either 8-PV/yr (a, c) or 80-PV/yr injection rate from the bottom fracture.

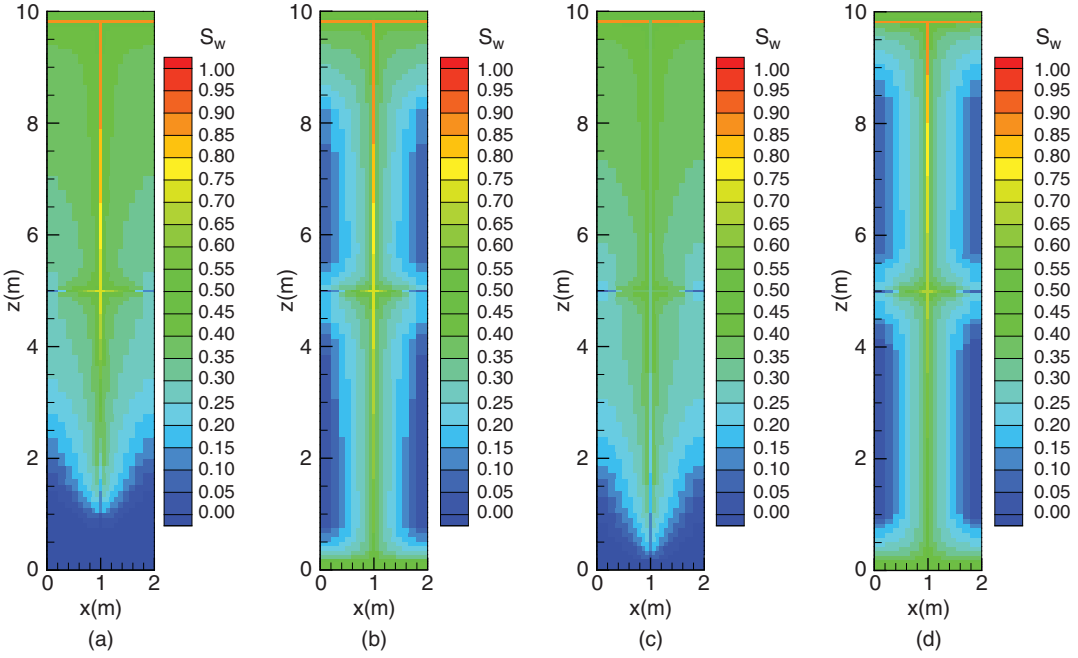

Fig. 13—Example 4: Water saturation at 0.3 PVI for simulations with capillarity and with fracture permeability of 4 darcies (a, b) and 100 darcies (c, d) and either 8-PV/yr (a, c) or 80-PV/yr injection rate from the top fracture.

TABLE 2—INITIAL COMPOSITIONS AND EOS PARAMETERS FOR ALL COMPONENTS IN EXAMPLE 5

Species	Composition, n (mol%)	Acentric Factor, ω	Critical Temperature, T_c (K)	Critical Pressure, P_c (bar)	Molar Weight, M_w (g/mol)	Critical Volume, V_c (cm^3/g)	Volume Shift Parameter, VSP	Nonzero Binary Interaction Coefficients With Respect to $C_1 + N_2$, $k_{C_1+N_2,j}$
H_2O	0.00	0.344	647	221	18	2.14	—	—
$C_1 + N_2$	0.57	0.012	189	46	16	6.09	–0.157	—
$C_2 - C_3$	0.16	0.120	330	46	35	4.73	–0.094	0.035
$C_4 - C_6$	0.08	0.233	455	35	69	4.32	–0.048	0.040
$C_6 - C_{10}$	0.09	0.428	584	24	120	4.25	0.055	0.048
C_{11+}	0.11	1.062	751	13	293	4.10	0.130	0.077

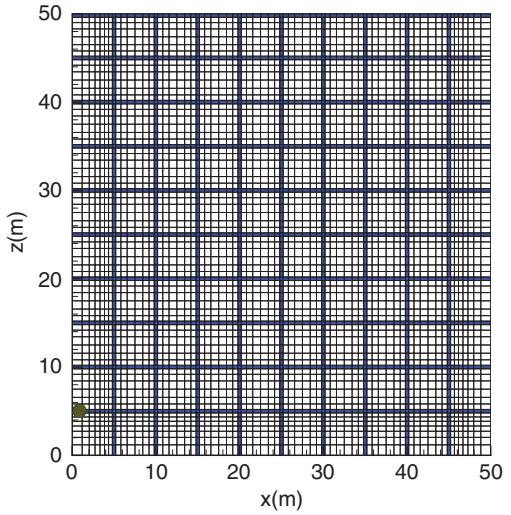

Fig. 14—Example 5a: Mesh and location of fractures and production well.

automatically. This phenomenon, which has challenged dual-porosity models, will be quantified in more detail in future work.

Example 6: Gravity Drainage, Water Imbibition, and CO_2 Injection in Fracture Domain. In the final example, we combine all the processes discussed so far in a compositional three-phase problem in a fractured domain, with both drainage and imbibition capillary pressures (with $\sigma_{wo} = 50$ dyne/cm). We consider the same setup as in Example 5a, but model depletion followed by waterflooding and then CO_2 injection. Specifically, the domain is depleted from the bottom for 4 years at 0.06 PV/yr until the pressure in the production well has dropped to 207 bar and a gas cap has developed in the top of the domain. In the next stage, 0.4 PV of water is injected from the bottom at a constant rate of 0.05 PV/yr and production is at a constant pressure from the top. The ROS to water is 50%, so we expect breakthrough to occur around this time through the fractures. In the final stage, the injection and production wells are switched and CO_2 is injected from the top at the same rate, with production from the bottom. The locations of injection and production wells are chosen on the basis of the relative densities of the fluids at the pressure of 207 bar, which is held constant during injection: $\rho_g = 164$ kg/m^3 $< \rho_{CO_2} = 394$ kg/m^3 $< \rho_o = 618$ kg/m^3 $< \rho_w = 949$ kg/m^3.

The gas saturation at the end of the depletion stage is similar to that shown in Figs. 19b and 20b. In the water-injection stage, there is three-phase flow and both imbibition (water/oil) and drainage (gas/oil) capillary pressures are considered. **Fig. 22** shows the water saturation at the end of water injection (0.4 PVI, 4 years) for simulations without and with capillarity. Similar to the previous examples, we find that imbibition drives considerable crossflow between the fractures and the matrix blocks and flow inside the matrix blocks. Although breakthrough has occurred without capillarity, in the simulation with capillary we see that the capillary-driven flow in the matrix blocks may exceed the convective flux in the fractures, delaying breakthrough.

Figs. 23 and 24 show, respectively, the water and gas saturation at one PVI (i.e., after depletion, 0.4 PVI of water injection, and 0.6 PVI of CO_2 injection; CPU time of approximately 12 hours). From the water saturation, we see that water production will be higher without capillarity. Because of the water/oil capillary pressure gradients, a substantial amount of water from imbibition remains trapped in the matrix blocks during CO_2 injection. The interpretation of the CO_2-injection stage is less straightforward because it depends on the combined effects of the flow of all three phases, both drainage and imbibition capillary pressures, as

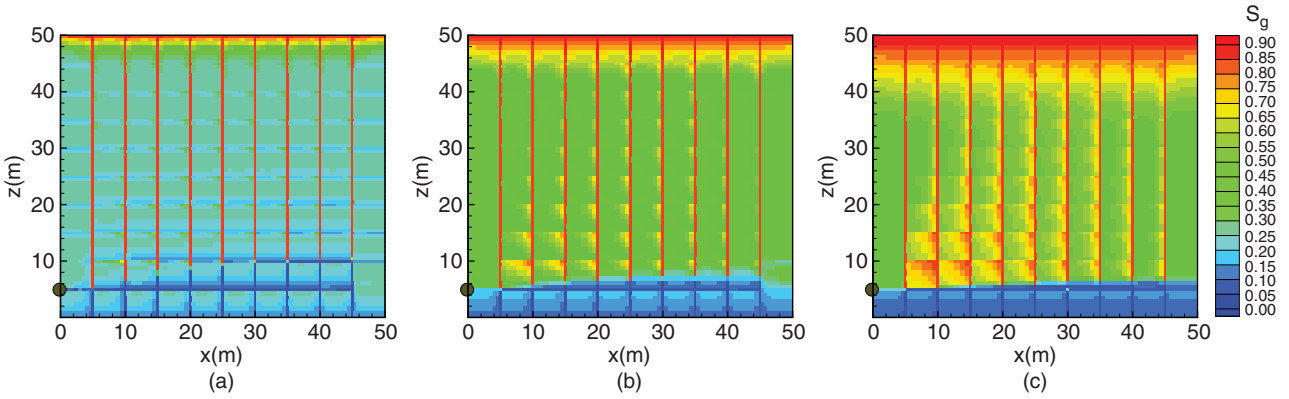

Fig. 15—Example 5a: Gas saturation for simulation without capillarity at 2 years (a), 5 years (b), and 10 years (c).

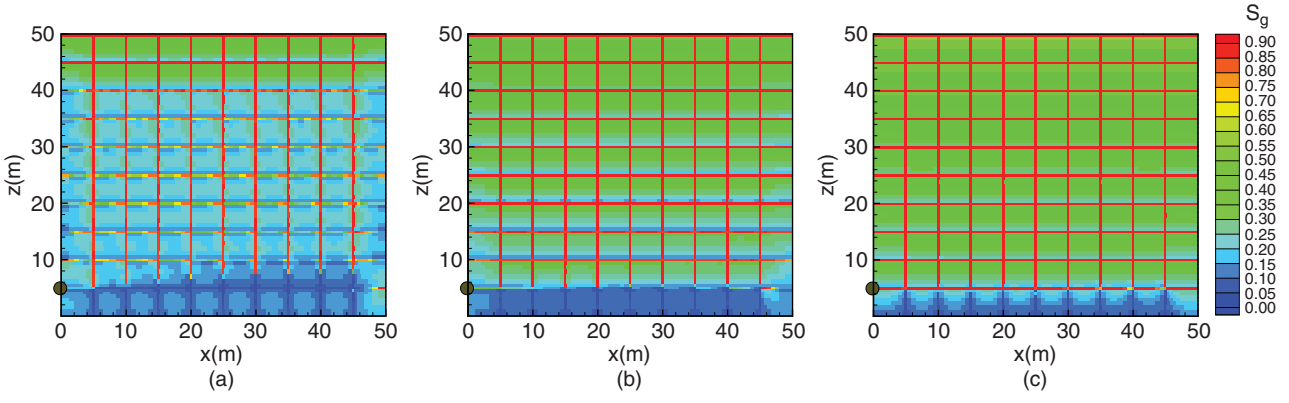

Fig. 16—Example 5a: Gas saturation for simulation with capillarity at 2 years (a), 5 years (b), and 10 years (c).

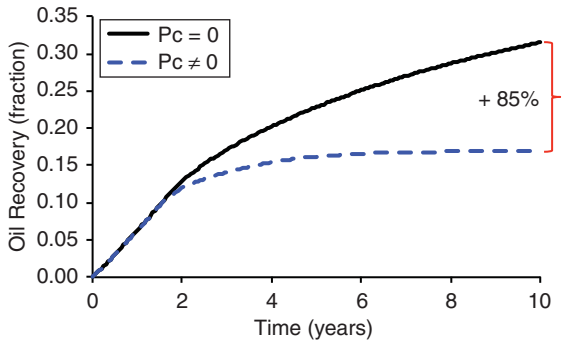

Fig. 17—Example 5a: Oil recovery with and without capillarity.

well as strong phase behavior. **Fig. 25** shows the oil and gas recoveries. The latter is the recovered fraction of the initial gas in place at surface conditions (i.e., produced CO_2 is subtracted). The gas/oil, water/oil, and water/gas (cumulative) ratios are given in **Fig. 26,** and the (instantaneous) overall compositions of water and CO_2 in the production well are shown in **Fig. 27.** The trends during depletion and waterflooding are clear. Oil recovery from depletion is higher without capillarity and gas/oil ratio is lower, caused by more-pronounced gravitational segregation. During water injection, first the gas cap is produced and the oil recovery is initially low, after which the recovery curve with capillarity is considerably steeper because of capillary imbibition. The earlier breakthrough time of water without capillarity is apparent in Fig. 27.

The higher oil recovery with capillarity during CO_2 injection is surprising. We carried out an additional simulation in which we

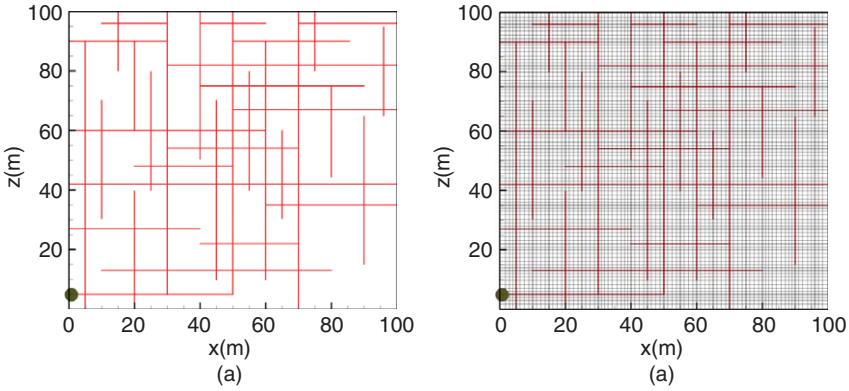

Fig. 18—Example 5b: Fracture configuration (a), mesh, and location of fractures and production well (b).

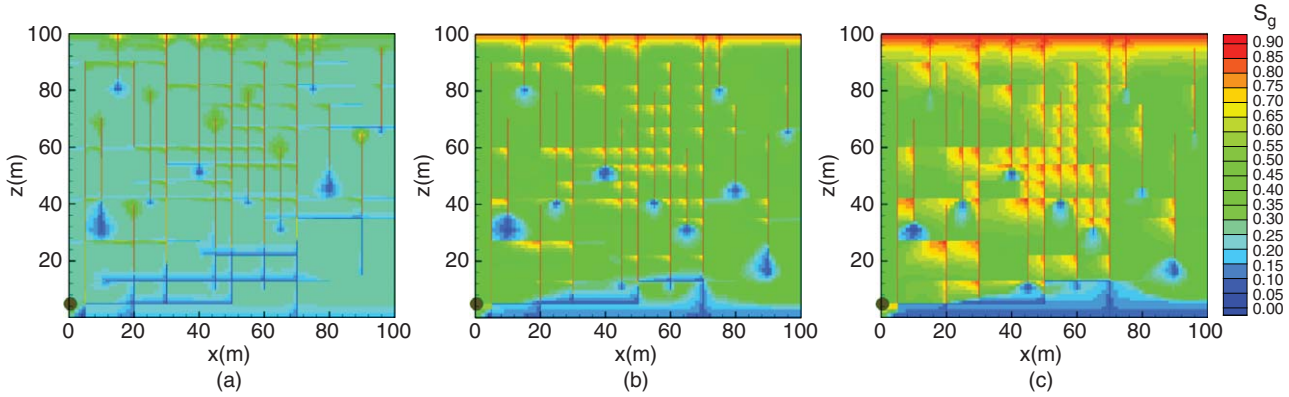

Fig. 19—Example 5b: Gas saturation for simulation without capillarity at 2 years (a), 5 years (b), and 10 years (c).

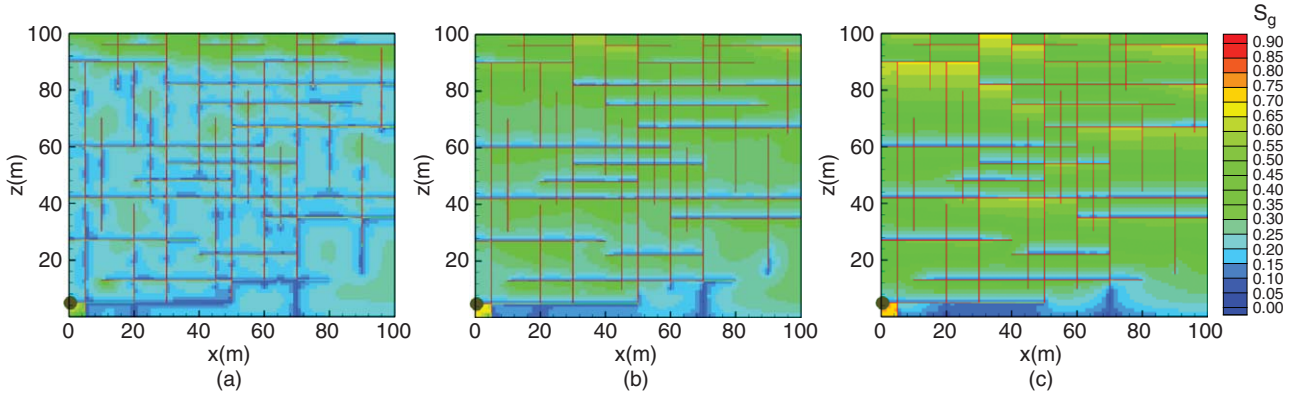

Fig. 20—Example 5b: Gas saturation for simulation with capillarity at 2 years (a), 5 years (b), and 10 years (c).

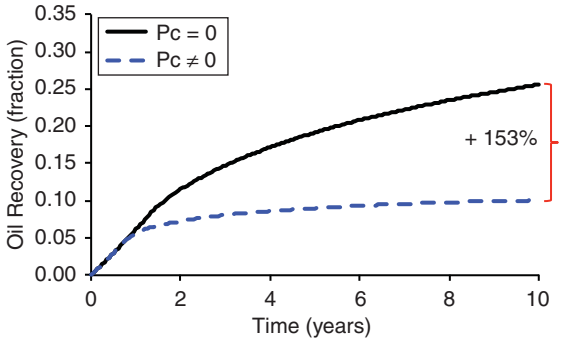

Fig. 21—Example 5b: Oil recovery with and without capillarity.

assume that the gas/oil capillary pressure is negligible for the CO_2-rich gas phase in the CO_2-injection stage (CO_2 has a high solubility of 56% in oil at 207 bar, and the surface tension is low at high pressures). We refer to the capillary pressures for the latter case by Pc2 in the figures. From carefully studying the production data (and Fig. 23), it is apparent that the higher oil recovery during the CO_2-injection stage from capillarity is because of the imbibition rather than the drainage capillary pressure. From the gas recovery (Fig. 25b), water- and gas-breakthrough times (Fig. 27), and water/gas ratio (Fig. 26) we find that the gas/oil capillary pressure does not strongly affect the flow of water and gas during CO_2 injection. Oil recovery is again negatively impacted by gas/oil capillary pressure: The vanishing capillary pressure in the fractures reduces the drainage of oil from the matrix blocks, similar to the capillary end-effect discussed in Example 1. This also

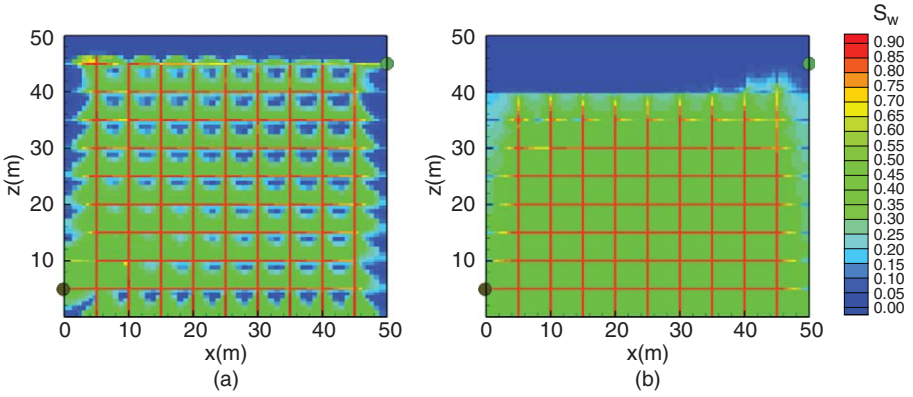

Fig. 22—Example 6: Water saturation at 0.4 PV of water injection without (a) and with capillary pressure (b).

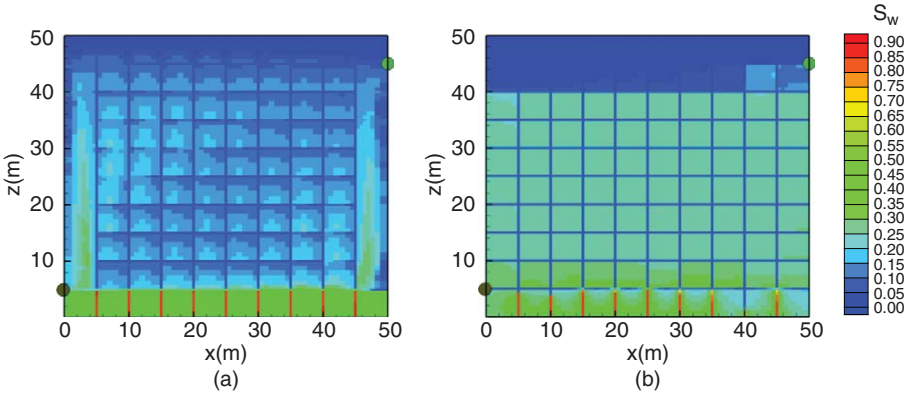

Fig. 23—Example 6: Water saturation at 0.4 PV of water and 0.6 PV of CO_2 injection without (a) and with capillary pressure (b).

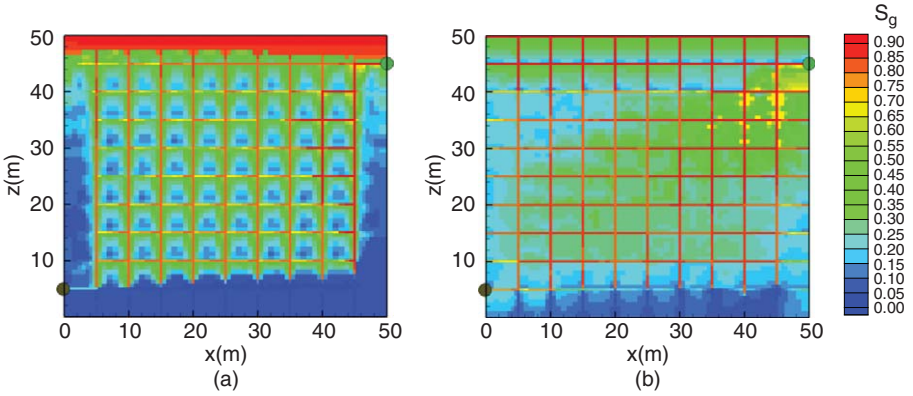

Fig. 24—Example 6: Gas saturation at 0.4 PV of water and 0.6 PV of CO_2 injection without (a) and with capillary pressure (b).

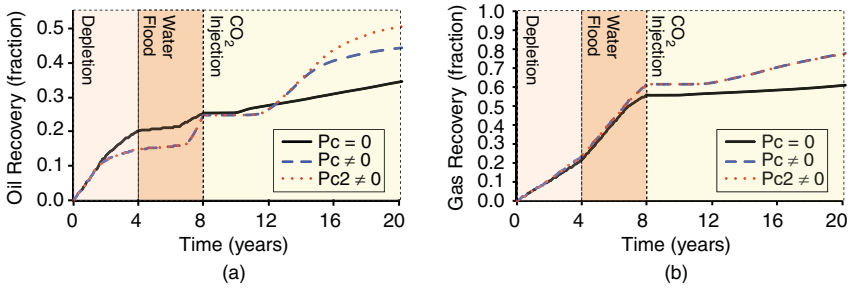

Fig. 25—Example 6: Oil (a) and gas (b) recovery with and without capillarity. Pc2 has zero gas/oil capillary pressure for CO_2-rich gas phase.

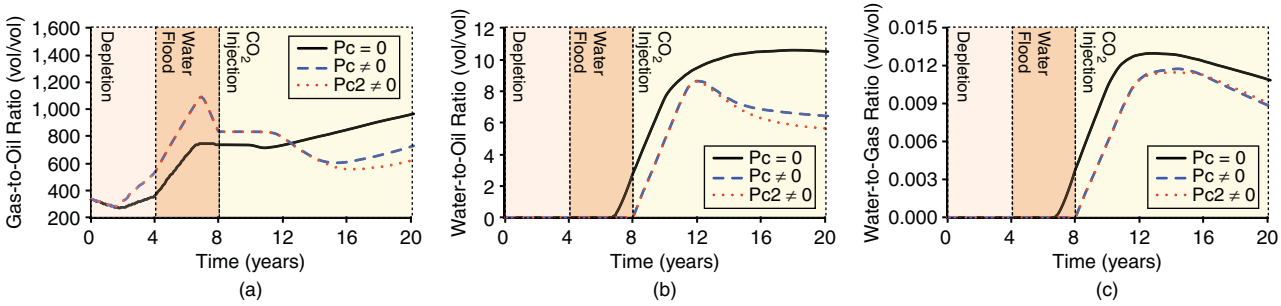

Fig. 26—Example 6: Gas/oil (a), water/oil (b), and water/gas ratios with and without capillarity. Pc2 has zero gas/oil capillary pressure for CO_2-rich gas phase.

explains the lower gas/oil and water/oil ratios for Pc2. The beneficial effect of imbibition capillary pressure can be seen in Figs. 26b, 26c, and 27a. To emphasize capillary effects, we have assumed no residual water saturations in this example. Without capillarity, most of the water from the waterflood is produced during CO_2 injection. Capillary pressure gradients at the fracture/matrix interface trap water in the matrix. Instead, oil drains from the matrix blocks, resulting in higher recovery.

We have attempted to reproduce aspects of Examples 4 through 6 with two of the most widely used commercial reservoir simulators. However, we find that they fail for problems of this complexity, because of both the phase behavior and the matrix inversion in the pressure solve with fractures. In a separate paper, we will compare less-complicated simulations with other models and experiments, where available, and study in more detail the effects of hysteresis and gravitational and capillary reinfiltration.

Conclusions

We have presented a model for capillarity in three-phase compositional flow in homogeneous, heterogeneous, and fractured porous media. The main features of the new formulation are

1. Both gas/oil and water/oil capillary pressures are considered.
2. The capillary pressure can be computed in each element from the phase saturations, rock properties, and a composition-dependent surface tension. Any tabular or functional dependence of relative permeabilities and capillary pressure on saturations can be readily accommodated.
3. The computation of capillary pressures at edges (particularly at interfaces between regions of different permeability) is based on the continuity of capillary pressures and fluxes. The gradients in capillary pressure, mobilities, and saturations, however, are discontinuous. From the cell-centered capillary pressure and the capillary pressures at the edges, the capillary pressure gradient can be computed within each element. In practice, only the capillary-driven flux $q^c \propto \lambda K \nabla p_c$ at the edges is required. These fluxes are derived, independent from the capillary pressure at the edges, from the harmonic average of the effective mobility λK and difference in capillary pressure between the neighboring elements.
4. For computational efficiency, we propose a fractional-flow formulation in terms of the total flux. The subsequent computations of the phase fluxes from the total flux depend on the upwind mobilities with respect to the phase fluxes, and that direction cannot be determined a priori when gravity and capillarity allow for countercurrent flow. We present an algorithm in which one phase direction can be determined from the gradients in potential differences, whereas the other two directions are the self-consistent solution of two trial orientations.
5. We can model capillarity in (discrete) fractured domains at approximately the same CPU efficiency as without capillarity.

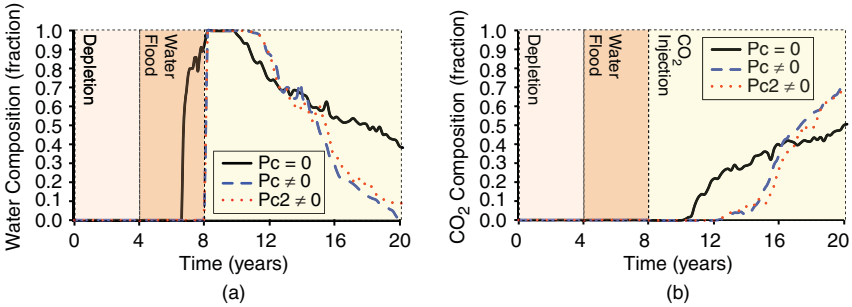

Fig. 27—Example 6: Overall water (a) and CO_2 (b) composition in production stream with and without capillarity. Pc2 has zero gas/oil capillary pressure for CO_2-rich gas phase.

The implementation of capillarity in fractured domains relies on the crossflow equilibrium concept. Fractures are combined with a small slice of the matrix on either side to form large computational elements. These larger elements alleviate the CFL condition on the timesteps and speed up the solver step for the pressures, because of the reduced contrast in size and effective permeability between matrix and fracture grid cells.

6. The model offers the benefits of earlier MHFE-DG implementations (without capillarity) in terms of low numerical-dispersion and grid-orientation effects, and an accurate continuous flux field across heterogeneities and fractures.

Nomenclature

$\mathbf{g}$ = gravitational acceleration vector
K = absolute permeability tensor
R = universal gas constant
T = (isothermal) temperature
ϕ = rock porosity (intrinsic porosity inside fractures is 1)

Phase Properties

c_α = molar density
$f_\alpha = \mathrm{k}_\alpha/\mathrm{k}_t$ = fractional flow function
$\tilde{f}_\alpha^{\mathrm{tot}}$ = fractional flow function from both fracture and matrix contributions in crossflow element
$\mathbf{G}_\alpha$ = auxiliary variable defined in Eq. 12
$\mathbf{J}_{i,\alpha}$ = diffusive flux
$\mathrm{k}_\alpha = \mathrm{K}\lambda_\alpha$ = effective mobility
$k_{r\alpha}$ = relative permeability
$\tilde{\mathrm{k}}_\alpha^{\mathrm{tot}}$ = effective mobility from both fracture and matrix contributions in crossflow element, as defined in Eq. 24
$K_{i,\alpha}$ = equilibrium ratio (Eq. 14)
p_α = pressure
S_α = saturation (volume fraction)
u_α = convective flux (Eq. 1)
VSP_α = volume shift parameter
$x_{i,\alpha}$ = species molar fraction
Z_α = compressibility factor
β_α = phase molar fraction
$\lambda_\alpha = k_{r\alpha}/\mu_\alpha$ = mobility
μ_α = viscosity
ρ_α = mass density
$\varphi_{i,\alpha}$ = fugacity coefficient

Properties in Multiphase Mixture

c = total molar density
F_i = sink/source term
$\|\mathrm{k}_{\mathrm{eff}}\|$ = weighted effective mobility across an edge E, as defined in Eq. 30
$\mathrm{k}_t = \Sigma_\alpha \mathrm{k}_\alpha$ = total effective mobility
$p_{c,go}$ = gas/oil capillary pressure (Eqs. 2 and 25)
$p_{c,gw}$ = gas/water capillary pressure
$p_{c,wo}$ = water/oil capillary pressure (Eqs. 3 and 26)
P_i = parachor
$S_{o,\mathrm{eff}}$ = effective oil saturation (Eq. 25)
S_{rg} = critical or residual gas saturation
S_{rog} = residual oil saturation to gas
S_{row} = residual oil saturation to water
S_{wc} = connate or residual water saturation
$S_{w,\mathrm{eff}}$ = effective water saturation (Eq. 26)
u_t = summed convective phase fluxes (Eq. 11)
U_i = total convective plus diffusive flux (Eq. 10)
$\overline{\nu}_i$ = total partial molar volume
z_i = total molar fraction
κ_T = total fluid compressibility (may also include rock compressibility)
σ_{go} = gas/oil surface tension (Eq. 27)
σ_{wo} = water/oil surface tension
Φ_{go} = gas/oil potential difference (Eq. 31)
Φ_{wg} = water/gas potential difference (Eq. 33)
Φ_{wo} = water/oil potential difference (Eq. 32)

Discretization Parameters

E = grid edge
K = grid element, with boundary ∂K
$n_{K,E}$ = outward normal with respect of edge E of element K
$p_{o,K}$ = element averaged oil pressure
$q_{\alpha,K,E}$ = discretized phase convective flux across E (given in Eq. 24 for a CF element)
$q^c_{go,K,E}$ = discretized gas/oil capillary contribution to the flux across E (Eq. 29)
$q^c_{wo,K,E}$ = discretized water/oil capillary contribution to the flux across E (similar to Eq. 29)
$q^{\mathrm{diff}}_{i\alpha,K,E}$ = discretized diffusive phase flux across E of species i
$q^g_{K,E}$ = discretized gravitational contribution to the flux across E
$q_{K,E}$ = discretized total convective flux across E (Eq. 18)
$tp_{o,K,E}$ = edge averaged oil pressure
$w_{K,E}$ = lowest-order Raviart-Thomas basis vector field
Δf = width of crossflow element
Δt = timestep
Δx = grid size
$\epsilon = \Delta f / |\mathrm{E}|$

Subscript

α = phase index
c = capillary
g = gas
go = gas/oil
i = species index
n_c = total number of components
o = oil
w = water
wg = water/gas
wo = water/oil

Superscript

c = capillary
f = fracture properties
g = gravitational
m = matrix properties
n = timestep
$\tilde{x}$ = upwind value of parameter x

Acknowledgments

We appreciate the support of this work by the member companies of the Reservoir Engineering Research Institute (RERI).

References

Acs, G., Doleschall, S., Farkas, E., 1985. General Purpose Compositional Model. *SPE J.* **25** (4): 543–553. http://dx.doi.org/10.2118/10515-PA.

Bentsen, R.G. and Anli, J., 1976. A New Displacement Capillary Pressure Model. *J. Cdn. Pet. Tech.* **15** (3): 75–79. http://dx.doi.org/10.2118/76-03-10.

Brooks, R., and Corey, A., 1964. Hydraulic Properties of Porous Media. *Hydrology Papers of Colorado State University* **3:**1–27.

Coats, K., 2003. IMPES Stability: Selection of Stable Timesteps. *SPE J.* **8** (2): 181–187. http://dx.doi.org/10.2118/84924-PA.

Corrêa, A.C.F., and Firoozabadi, A., 1996. Concept of Gravity Drainage in Layered Porous Media. *SPE J.* **1** (1): 101–111. http://dx.doi.org/10.2118/26299-PA.

Courant, R., Friedrichs, K. and Lewy, H., 1928. Partial Differential Equations of Mathematical Physics. *Math. Ann.* **100** (1): 32–74. http://dx.doi.org/10.1007/BF01448839.

Davis, T.A., 2004. A Column Pre-Ordering Strategy for the Unsymmetric-Pattern Multifrontal Method. *ACM T. Math. Software* **30** (2): 165–195. http://dx.doi.org/10.1145/992200.992205.

Geiger, S., Matthäi, S., Niessner, J., et al. 2009. Black-Oil Simulations for Three-Components, Three-Phase Flow in Fractured Porous Media. *SPE J.* **14** (2): 338–354. http://dx.doi.org/10.2118/107485-PA.

Hadley, G. and Handy, L., 1956. A Theoretical and Experimental Study of the Steady State Capillary End Effect. Paper SPE 707-G presented at the Fall Meeting of the Petroleum Branch of AIME, Los Angeles, California, 14–17 October. http://dx.doi.org/10.2118/707-G.

Hoteit, H. and Firoozabadi, A. 2005. Multicomponent Fluid Flow by Discontinuous Galerkin and Mixed Methods in Unfractured and Fractured Media. *Water Resour. Res.* **41** (11): W11412. http//dx.doi.org/10.1029/2005WR004339.

Hoteit, H. and Firoozabadi, A. 2006a. Compositional Modeling by the Combined Discontinuous Galerkin and Mixed Methods. *SPE J.* **11** (1): 19–34. http://dx.doi.org/10.2118/90276-PA.

Hoteit, H. and Firoozabadi, A. 2006b. Compositional Modeling of Discrete-Fractured Media without Transfer Functions by the Discontinuous Galerkin and Mixed Methods. *SPE J.* **11** (3): 341–352. http://dx.doi.org/10.2118/90277-PA.

Hoteit, H. and Firoozabadi, A. 2008a. An Efficient Numerical Model for Incompressible Two-Phase Flow in Fractured Media. *Adv. Water Resour.* **31** (6): 891–905. http://dx.doi.org/10.1016/j.advwatres.2008.02.004.

Hoteit, H. and Firoozabadi, A. 2008b. Numerical Modeling of Two-Phase Flow in Heterogeneous Permeable Media with Different Capillarity Pressures. *Adv. Water Resour.* **31** (1): 56–73. http://dx.doi.org/10.1016/j.advwatres.2007.06.006.

Huang, D.D. and Honarpour, M.M. 1998. Capillary End Effects in Coreflood Calculations. *J. Pet. Sci. Eng.* **19** (1): 103–117. http://dx.doi.org/10.1016/S0920-4105(97)00040-5.

Hustad, O. and Browning, D. 2010. A Fully Coupled Three-Phase Model for Capillary Pressure and Relative Permeability for Implicit Compositional Reservoir Simulation. *SPE J.* **15** (4): 1003–1019. http://dx.doi.org/10.2118/125429-PA.

Moinfar, A., Varavei, A., Sepehrnoori, K., et a. 2012. Development of a Novel and Computationally-Efficient Discrete-Fracture Model to Study IOR Processes in Naturally Fractured Reservoirs. Paper SPE 154246 presented at the SPE Improved Oil Recovery Symposium, Tulsa, Oklahoma, 14–18 April. http://dx.doi.org/10.2118/154246-MS.

Moortgat, J. and Firoozabadi, A. 2010. Higher-Order Compositional Modeling with Fickian Diffusion in Unstructured and Anisotropic Media. *Adv. Water Resour.* **33** (9): 951–968. http://dx.doi.org/10.1016/j.advwatres.2010.04.012.

Moortgat, J. and Firoozabadi, A. 2012. In press. Higher-Order Compositional Modeling of Three-phase Flow in Fractured Reservoirs Using Cross-Flow Equilibrium Approach. Journal of Computational Physics (submitted 4 April 2013).

Moortgat, J., Firoozabadi, A., Li, Z., et al. 2013. CO_2 Injection in Vertical and Horizontal Cores: Measurements and Numerical Simulation. *SPE J.* (in press; published online 31 January 2013). http://dx.doi.org/10.2118/135563-PA.

Moortgat, J., Firoozabadi, A. and Moravvej Farshi, M. 2009. A New Approach to Compositional Modeling of CO_2 Injection in Fractured Media Compared to Experimental Data. Paper SPE 124918 presented at the SPE Annual Technical Conference and Exhibition, New Orleans, Louisiana, 4–7 October. http://dx.doi.org/10.2118/124918.

Moortgat, J., Li, Z. and Firoozabadi, A. 2012. Three-Phase Compositional Modeling of CO_2 Injection by Higher-Order Finite Element Methods with CPA Equation of State for Aqueous Phase. *Water Resour. Res.* **48** (12): W12511. http://dx.doi.org/10.1029/2011WR011736.

Moortgat, J., Sun, S. and Firoozabadi, A. 2011. Compositional Modeling of Three-Phase Flow with Gravity Using Higher-Order Finite Element Methods. *Water Resour. Res.* **47** (5): W05511. http://dx.doi.org/10.1029/2010WR009801.

Raviart, P.A. and Thomas, J.M. 1977. Primal Hybrid Finite-Element Methods for Second-Order Elliptic Equations. *Math. Comput.* **31** (138): 391–413.

Tan, C. and Firoozabadi, A. 1995a. Theoretical Analysis of Miscible Displacement in Fractured Porous Media by a One-Dimensional Model: Part I–Theory. *J. Cdn. Pet. Tech.* **34** (2):17–27. http://dx.doi.org/10.2118/95-02-01.

Tan, C. and Firoozabadi, A. 1995b. Theoretical Analysis of Miscible Displacement in Fractured Porous Media by a One-Dimensional Model: Part II–Features. *J. Cdn. Pet. Tech.* **34** (2): 29–35. http://dx.doi.org/10.2118/95-02-02.

Watts, J.W. 1986. A Compositional Formulation of the Pressure and Saturation Equations. *SPE Res Eng* **1** (3): 243–252. http://dx.doi.org/10.2118/12244-PA.

Yokoyama, Y. and Lake, L.W. 1981. The Effects of Capillary Pressure on Immiscible Displacements in Stratified Porous Media. Paper SPE 10109 presented at the SPE Annual Technical Conference and Exhibition, San Antonio, Texas, 4–7 October. http://dx.doi.org/10.2118/10109-MS.

Appendix A: Coefficients in MHFE Expansion of Convective Fluxes and Pressures

The $\beta_{K,E,E'}$ and $\theta_{K,E}$ coefficients in Eq. 18 are given by

$$\beta_{K,E,E'} = \lambda_{t,K}\left(\int_K w_{K,E}\mathrm{K}_K^{-1}w_{K,E'}\right)^{-1} \quad \text{and} \quad \theta_{K,E} = \sum_{E'}\beta_{K,E,E'}. \qquad \text{(A-1)}$$

To provide the coefficients in Eq. 20, we first introduce the notation

$$\begin{aligned} m_{i,K,E} &= \sum_{\alpha} c_{\alpha,K,E}x_{i,\alpha,K,E}f_{a;K;E},\\ \tilde{v}_{K,E} &= \sum_{i=1}^{n_c}\overline{v}_i m_{i,K,E}, \quad \text{and}\\ \boldsymbol{s}_{i,K} &= \sum_{\alpha} c_{\alpha,K,E}x_{i,\alpha,K,E}f_{a;K;E}\mathbf{G}_{\alpha,K,E}, \end{aligned} \qquad \text{(A-2)}$$

where $\tilde{s}_{i,K,E} = \int_E \mathbf{s}_{i,K}\cdot\mathbf{n}_{K,E}$ and $c_{\alpha,K,E}$, $x_{i,\alpha,K,E}$, and $f_{a;K;E}$ are the molar density, molar composition, and fractional flow function evaluated at edge E, respectively. The contributions from capillarity are incorporated in $\boldsymbol{G}_{\alpha,K,E}$, from Eq. 12, with capillary pressure gradients at each edge E written in terms of discretized $q^c_{go,K,E}$ and $q^c_{wo,K,E}$ terms. The coefficients in Eq. 20 are expressed in terms of the previously discussed definitions as

$$\begin{aligned} &\tilde{\alpha}_K = \sum_{E\in K}\tilde{v}_{K,E}\theta_{K,E}, \quad \tilde{\beta}_{K,E} = \sum_{E'\in\partial K}\tilde{v}_{K,E}\beta_{K,E,E'}, \quad \text{and}\\ &\tilde{\gamma}_K = \sum_{E\in\partial K}\left(\tilde{v}_{K,E}\gamma_{K,E} + \sum_{i=1}^{n_c}\overline{v}_i\tilde{s}_{i,K,E}\right). \end{aligned} \qquad \text{(A-3)}$$

For N_K grid elements and N_E edges, $\mathbf{P}$ is the N_K-sized vector of element-averaged oil pressures and $\mathbf{T}_P$ is a N_E-sized vector of the oil pressure traces at all the edges. For the global MHFE system of equations, the coefficients in Eqs. A-1 and A-3 are collected in the following matrices:

$$R \in \mathbb{R}^{N_K N_E}, \quad R_{K,E} = \theta_{K,E}, \qquad \text{(A-4)}$$

$$M \in \mathbb{R}^{N_E, N_E}, \quad M_{E,E'} = \sum_{K:E,E'\in\partial K}\beta_{K,E,E'} \qquad \text{(A-5)}$$

$$I \in \mathbb{R}^{N_E}, \quad I_E = \sum_{K:E\in\partial K}\gamma_{K,E} \qquad \text{(A-6)}$$

$$D \in \mathbb{R}^{N_K,N_K}, \quad D_{KK} = \frac{\kappa_T\phi|K|}{\Delta t} + \tilde{\alpha}_K \qquad \text{(A-7)}$$

$$\tilde{R} \in \mathbb{R}^{N_K N_E}, \quad \tilde{R}_{K,E} = \tilde{\beta}_{K,E} \qquad \text{(A-8)}$$

$$G \in \mathbb{R}^{N_K}, \quad G_K = \kappa_T\phi|K|\frac{p_K(t_{\text{old}})}{\Delta t} + \tilde{\gamma}_K. \qquad \text{(A-9)}$$

Joachim Moortgat is currently an assistant professor at the School of Earth Sciences, Ohio State University. This work was carried out during a postdoctoral research position at RERI. His research interests are in the theory and advanced numerical

modeling of compositional multiphase flow in subsurface fractured porous media. Moortgat holds MS degrees in theoretical physics and astrophysics, both from Utrecht University, the Netherlands, and a PhD degree in astrophysics from the Radboud University, the Netherlands.

Abbas Firoozabadi is the senior scientist and director at RERI. He also teaches at Yale University. Firoozabadi's main research activities center on thermodynamics of hydrocarbon reservoirs and production and on multiphase/multicomponent flow in fractured petroleum reservoirs. He holds a BS degree from the Abadan Institute of Technology, Abadan, Iran, and MS and PhD degrees from the Illinois Institute of Technology, Chicago, all in gas engineering. Firoozabadi is the recipient of the 2002 SPE/AIME Anthony Lucas Gold Medal and is a member of the National Academy of Engineering.